



TECHNISCHE
UNIVERSITÄT
WIEN
Vienna | Austria

DIPLOMARBEIT

Influence of external magnetic perturbations on the plasma boundary in L-mode and on the plasma position control system of ASDEX Upgrade

Ausgeführt am
Institut für Angewandte Physik
der Technischen Universität Wien
und
Max-Planck-Institut für Plasmaphysik
in Garching

unter der Anleitung von
Univ.Prof. Dr. Friedrich Aumayr
Dr. Matthias Willensdorfer
Univ.Doz. Dr. Elisabeth Wolfrum

durch
Jakob Kirschner
Matrikelnummer 0825571
Am Ipfbach 47, A-4490 St. Florian

Abstract

The currently most developed concept for a fusion reactor is the Tokamak, but some challenges still need to be solved. The high confinement mode, in which future Tokamaks are thought to be operated, is susceptible to plasma instabilities called edge localized modes (ELMs). These modes can lead to a sudden exhaust of particles and energy, too high for the material of the plasma facing components to withstand. One approach to mitigate or suppress ELMs is to perturb the magnetic field at the plasma edge with perturbation coils. These magnetic perturbations break the toroidal symmetry of a Tokamak and can also influence the plasma position control system. For future machines the perturbations could lead to problems concerning minimum wall distances needed for safe operation.

In this thesis the corrugation of flux surfaces and the induced movement due to the plasma position control system is obtained from measurements and subsequently compared to simulations by VMEC, a code that includes the plasma response to the magnetic perturbations and vacuum field line tracing. This is done to investigate the behavior of the control system and to test the predictability of simulations for future machines. The analyzed discharges were done at ASDEX Upgrade in L-mode and the diagnostics used are the lithium beam diagnostic and magnetic probes arranged in two arrays measuring the poloidal magnetic field at two toroidally shifted positions. The perturbations are rigidly rotated to allow for 2D measurements with 1D diagnostics or 3D with 2D. The lithium beam diagnostic gives electron density profiles which allows us to estimate the separatrix position through tracing a certain density over time. The equilibrium reconstruction based on Bayesian analysis is using the magnetic measurements to obtain the axisymmetric poloidal flux which in turn allows us to trace the separatrix.

A phase relation between the obtained corrugation and the measured magnetic field in a poloidal flux probe is found. This could be a hint that stray fields from the perturbation coils influence the position control system. The movement due to the control system and the corrugation show an amplitude in the one-digit mm range with slightly varying phase differences. The VMEC results show a good agreement for the discharges with $n=2$, especially for the fundamental harmonic of the corrugation and no agreement for the higher harmonics. The vacuum field line tracing shows a reasonable agreement, better for the discharges with non-resonant perturbations. A discharge with $n=1$ and a rotating locked mode shows no agreement between measurement and simulations.



Kurzfassung

Das derzeit am weitesten entwickelte Konzept für einen Fusionsreaktor ist der Tokamak, bei dem allerdings noch bestimmte Probleme auftreten. Die H-Mode (high confinement mode), in der nach derzeitigem Stand, zukünftige Tokamaks betrieben werden, ist anfällig für ELM (edge localized mode) genannte Plasmainstabilitäten. Diese Moden können einen Energie- und Teilchentransport verursachen, dem derzeitige Wandmaterialien nicht standhalten würden. Ein Ansatz um ELMs abzuschwächen oder zu unterdrücken ist die Störung des Magnetfeldes am Plasmarand durch Störspulen. Diese Störungen brechen die toroidale Symmetrie eines Tokamaks und können auch das Plasmapositionskontrollsystem beeinflussen. Für zukünftige Maschinen könnte dies zu Problemen mit dem Minimalabstand zwischen Plasma und Wand, der für einen sicheren Betrieb nötig ist, führen.

In dieser Arbeit wird die Störung der Flussflächen und die induzierte Bewegung des Kontrollsystems aus Messungen errechnet und anschließend mit VMEC, einem Code der die Reaktion des Plasmas auf die externen Störungen berücksichtigt und Vakuum Feldlinienverfolgungssimulationen verglichen. Dies wird getan um das Verhalten des Kontrollsystems und die Vorhersagbarkeit von Simulationen für zukünftige Maschinen zu analysieren. Die untersuchten Plasmaentladungen wurden an ASDEX Upgrade in L-Mode durchgeführt und die verwendeten Diagnostiken sind die Lithiumstrahl Diagnostik und magnetische Sonden, welche in zwei toroidal verschobenen Ringen angeordnet sind. Die Störfelder wurden starr rotiert, um 2D Messungen mit einer 1D Diagnostik bzw. 3D Messungen mit 2D Diagnostiken durchzuführen. Die Lithiumstrahl Diagnostik liefert Profile der Elektronendichte, mit welchen die Separatrix über die Dichte verfolgt werden kann. Die Gleichgewichtsrekonstruktion, basierend auf Bayes'scher Wahrscheinlichkeitsrechnung, verwendet die magnetischen Messungen um den axisymmetrischen poloidalen Fluss zu bestimmen, mit welchem die Separatrix verfolgt werden kann.

Eine Phasenbeziehung zwischen der gemessenen Verformung und dem gemessenen magnetischen Feld einer Poloidalfeld-Sonde wurde gefunden. Dies könnte darauf hinweisen, dass die Streufelder der Störspulen das Kontrollsystem beeinflussen. Die Bewegung des Kontrollsystems und die Verformung zeigen Amplituden im einstelligen mm-Bereich mit leicht variierenden Phasenunterschieden. Die VMEC Ergebnisse zeigen eine gute Übereinstimmung mit den $n=2$ Entladungen, vor allem für die Fundamentalschwingung und keine Übereinstimmung für die höheren Harmonischen. Die Vakuumfeld-Näherung zeigt eine akzeptable Übereinstimmung mit den Messungen, die bei den nicht-resonanten Schüssen etwas besser ist. Eine $n=1$ Entladung mit einer rotierenden gebundenen Mode zeigt keine Übereinstimmung zwischen Messung und Simulationen.



Contents

1	Introduction	1
1.1	Nuclear Fusion and Magnetic Confinement	1
1.2	The Tokamak	3
1.3	H-Mode and Edge Localized Modes	5
1.4	External Magnetic Perturbations	8
1.5	Motivation	8
2	Theory and Modeling	11
2.1	Magnetohydrodynamics	11
2.1.1	Basics	11
2.1.2	Equilibrium	12
2.1.3	Linear Stability	13
2.2	VMEC	15
2.3	Vacuum field line tracing	16
3	Experimental Setup and Diagnostics	19
3.1	ASDEX Upgrade	19
3.2	External Magnetic Perturbation Coils	20
3.3	The Lithium Beam Diagnostic	21
3.4	B_θ Arrays	23
3.5	The Plasma Control System	23
3.6	Integrated Data Equilibrium	24
4	Method	27
4.1	Rigid Rotation	27
4.2	Measurement of the Displacement	28
4.3	Estimation of the Axisymmetric Movement	31
4.4	Consistency of Method	33
4.5	Set of Analyzed Discharges	37
5	Role of the Plasma Position Control	39
5.1	Behavior, currents B_{pslur} vs CL	39
5.2	Estimation of the 3D Components on the Axisymmetric Equilibrium	41
6	Results	45
6.1	$n=2$ Comparison and Side Bands	45
6.2	$n=2$ Comparison with Different Coil Configurations	46
6.3	Density Scan	48
6.4	$n=1$ Comparison	50
7	Discussion	53
A	Acknowledgement	55
B	Bibliography	57

CONTENTS

1 Introduction

1.1 Nuclear Fusion and Magnetic Confinement

The growing energy demand of humanity and climate change associated with the combustion of fossil fuels call for new technologies as an alternative to conventional sources of energy. A good mix of emission free energy carriers is needed, if we want to keep our way of living without destroying the environment. One component of this mix could be realized by nuclear fusion power plants. Once they are available they could replace conventional fission power plants. Due to their advantages concerning security and nuclear waste, the concept of fusion is far superior than the one of fission. For fission, the challenge is to control a nuclear chain reaction with potential fuel for years being inside the reactor, while in fusion reactors the desired reaction is challenging and even more difficult to sustain for a sufficient amount of time. Therefore any failure would lead to the stoppage of the reaction and with enough fuel for only a couple of seconds inside the reaction vessel a fusion reactor is inherently safe. Other advantages are that the produced exhaust gas is Helium and the short term waste is reduced to a minimum.

As the name already suggests the energy in a fusion reactor comes from fusing light nuclei to heavier ones. There are different possible fusion reactions suitable for gaining energy in a reactor. With a maximum of the cross section at a relative energy of 100 keV, the DT-reaction,



is the easiest to achieve. This would correspond to a temperature of about 10^9 K. However, sufficiently high reaction rates can already be achieved by heating the DT-mixture to about 10^8 K (10 keV). This is due to the Maxwellian velocity distribution where at lower temperatures also particles with higher energies are present. To produce a net energy gain in a fusion reactor, the Lawson criterion for DT-plasmas at $T=15$ keV:

$$n T \tau_E > 3 \times 10^{21} \text{ keV} \cdot \text{s} \cdot \text{m}^{-3}, \quad (2)$$

has to be fulfilled [1]. It states that the triple product of density n , temperature T and energy confinement time τ_E has to be above a certain value and already considers the energy conversion from thermal to electrical energy. The energy confinement time is defined by $\tau_E = W/P_{\text{loss}}$, where W is the total energy stored in the plasma and P_{loss} the rate of energy loss.

At these high temperatures the state of matter is plasma and it's obvious that there is no material to withstand direct contact. However, the plasma has to either be dense enough or confined long enough for a sufficient amount of fusion reactions to occur. There are two main concepts to do so and fulfill the Lawson criterion: Inertially confined fusion and magnetically confined fusion. The former one uses frozen DT-pellets and heats their surface as uniformly as possible with a short laser or heavy ion beam pulse. This intense heating creates an inward implosion due to the explosion and ablation of the outermost layer. High densities of about 10^{31} m^{-3} are reached for a short time of about 10^{-10} s.

On the other hand magnetic confinement uses the fact that a plasma consists of charged particles and therefore magnetic fields can be used to trap them. It aims for a longer confinement time in the order of seconds at lower densities of about 10^{20} m^{-3} . In the beginning, linear magnetic configurations were used to trap the particles. As it turned out the loss of particles at the ends was too high to achieve an acceptable quality of confinement. Therefore the next idea was to bend these linear devices, connect the ends to each other and get a toroidal configuration. However, a purely toroidal configuration is also not efficient for a high confinement time.

A first explanation of how the confinement works in toroidal magnetic fields can be given by the one particle model. The trajectory of a single charged particle in a static magnetic field is studied using the Lorentz force. This means that we neglect the fields from the other moving plasma particles and the collisions that inevitably happen between the particles. In a purely toroidal magnetic field certain drift movements occur. It can be shown that in an inhomogeneous magnetic field the ∇B -drift:

$$\vec{v}_{\nabla B} = -\frac{\mu_m}{q} \frac{\nabla B \times \vec{B}}{B^2}, \quad (3)$$

and curvature drift:

$$\vec{v}_c = \frac{mv_{\parallel}^2}{qB^2} \frac{\vec{R}_c \times \vec{B}}{R_c^2}, \quad (4)$$

appear [2]. v_{\parallel} is the velocity parallel to the magnetic field, \vec{R}_c the radius of the curvature, μ_m the magnetic moment, q the charge and m the mass of the particle. Both drift movements point in the same direction and lead to a charge separation between electrons and ions. This charge separation creates an electric field in the plasma which in turn leads to the radially outward pointing $\vec{E} \times \vec{B}$ drift:

$$\vec{v}_{\vec{E} \times \vec{B}} = \frac{\vec{E} \times \vec{B}}{B^2}. \quad (5)$$

Since this drift movement is charge independent it would lead to a high radially outward pointing transport and the sudden loss of the plasma particles hitting the wall. To circumvent this problem a poloidal component perpendicular to the toroidal field is added to the magnetic field. The charge separating movement gets compensated over one poloidal turn and confinement is possible. The poloidal component is either generated by specially shaped coils like in a Stellarator or generated by a toroidal current which leads to the Tokamak concept.

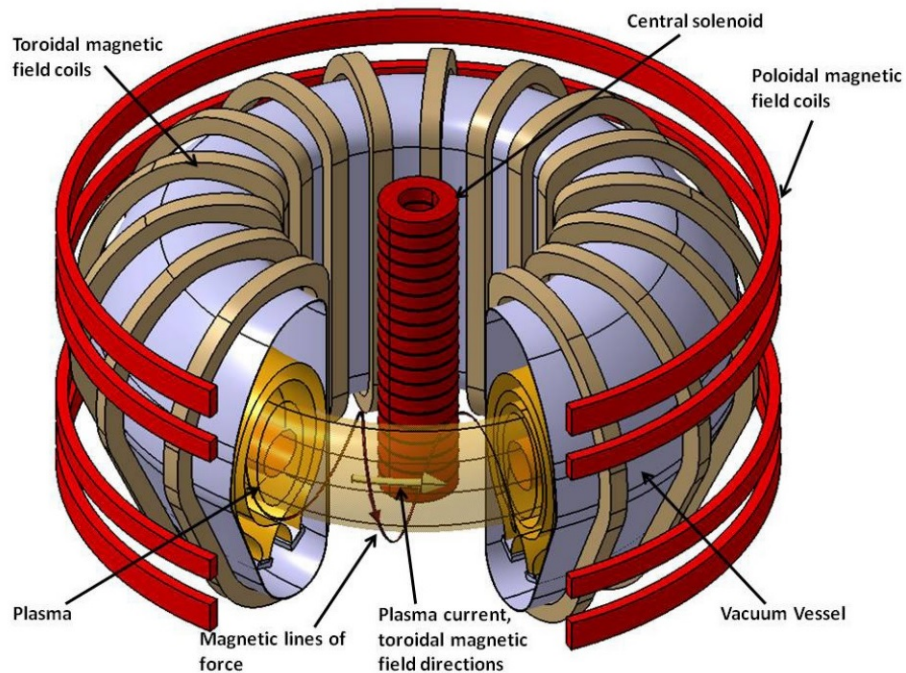


Figure 1: Tokamak configuration, the slope of the magnetic field in real machines is a lot lower which translates to a higher safety factor [3, p.28].

1.2 The Tokamak

In a Tokamak reactor the plasma vessel has the shape of a torus and is wrapped around a central solenoid as shown in Fig. 1. The set of toroidal magnetic field coils create a magnetic field in toroidal direction. The toroidal current which is necessary to obtain the poloidal field component is induced by a change of the current through the central solenoid. The plasma acts as a secondary transformer winding with the central solenoid acting as a part of the transformer core. This leads to the problem that a Tokamak can only be operated in pulses, if no other current drives are used. In so-called advanced Tokamak scenarios one goal is to drive the current non-inductively, preferably by a combination of an intrinsic plasma generated current and currents from externally applied heating systems [4]. Additional poloidal field coils are installed to control the position and the shape of the plasma.

Figure 2 shows the toroidal coordinates and magnetic field lines. Following one magnetic field line over numerous circulations around the torus it always stays on a surface with constant magnetic flux. These so-called flux surfaces are nested around the magnetic axis and particles can move perpendicular to them only by collisions with other charged particles or through turbulence.

An important plasma parameter is the safety factor q shown in eq. 6, which gives the number of toroidal turns per poloidal turn. It is named after the immense importance it plays in determining MHD stability, as will be shown in chapter 2.1.

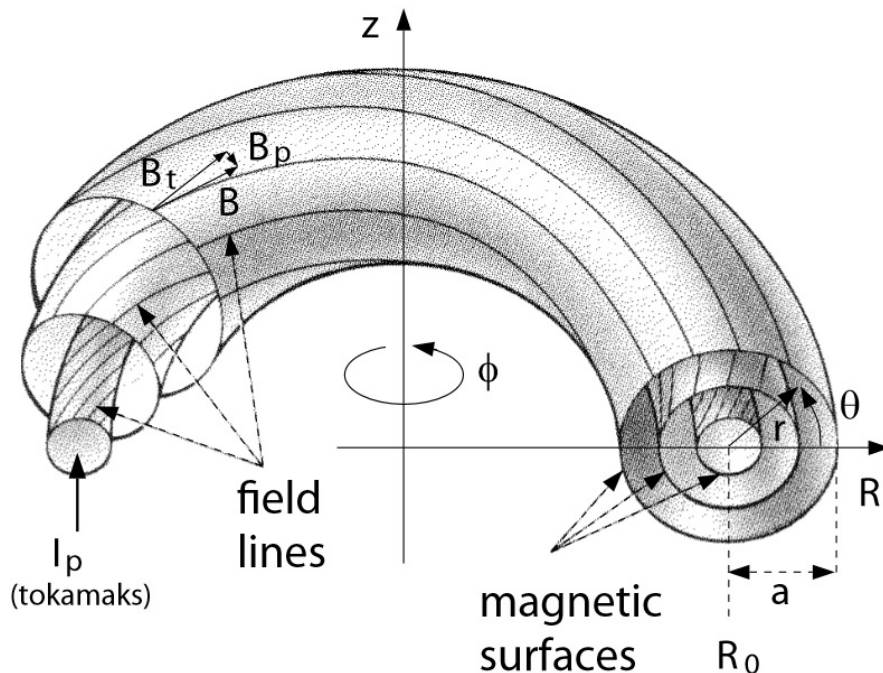


Figure 2: R_0 is also called the major plasma radius and a the minor one. B_p is the magnetic field in poloidal direction and B_t in the toroidal direction [5].

$$q = \frac{\Delta\Phi}{2\pi} \simeq \frac{rB_t}{R_0B_p}, \quad (6)$$

where $\Delta\Phi$ is the change of toroidal angle per poloidal turn and B_t and B_p the toroidal and poloidal magnetic field respectively. The approximation is valid for a tokamak with a circular cross section and a large aspect ratio R_0/r , where R_0 is the big plasma radius and r the small one.

$$s = \frac{r}{q} \frac{dq}{dr} \quad (7)$$

is another quantity relevant for plasma stability and is called the magnetic shear which is defined by the radial change of q (eq. 7). In general a high shear ensures better stability. The topic of stability will be explained in more detail in chapter 2.1. For now a short discussion about the radial transport across the flux surfaces will be given.

Starting point is the classical diffusion where collisions between particles lead to a diffusion that is related to the gyro radius of the respective particles. Only taking into account classical diffusion, an estimation of the small plasma radius for a fusion reactor to reach a net energy gain is about 7 mm [6]. However, other effects play a significant role in reducing the quality of confinement and increase the diffusion coefficient by some orders of magnitude. The so-called neoclassical diffusion, occurs because of the existence of trapped particles. Due to symmetry reasons the strength of the toroidal magnetic field decreases with the radius ($B_t \propto 1/R$). Therefore, the plasma in a Tokamak can be divided into a high field side which is located

radially inward of the magnetic axis and a low field side located radially outward of it. Particles with not high enough energies can be reflected on the high field side similar to a magnetic bottle. Projecting the trajectory of such a trapped particle onto a poloidal plane gives a banana shape. The width of these so-called banana orbits is one order of magnitude higher than the gyro radius [2]. If a trapped particle collides, its trajectory changes by the width of the banana instead of a gyro radius. Hence the diffusion increases.

However this doesn't yet explain the highly increased diffusion observed in experiments. Nowadays theory tries to explain this so-called anomalous transport by non-linear turbulence models. With these descriptions diffusion coefficients of the same order of magnitude as the experimental ones can be obtained. This furthermore leads to an estimated small plasma radius of 2,2 m and the big size of ITER (the biggest Tokamak, currently under construction).

In comparison to the transport perpendicular to the flux surfaces, the parallel transport is highly increased and particles can move almost freely along the field lines. This allows us to guide the exhaust particles to the so-called Divertor which has been proven useful to catch and remove the plasma particles from the vessel and therefore keep the plasma clean from impurities. Figure 3 shows a poloidal cross section of the plasma in a Tokamak. On the inside, the magnetic surfaces are closed with the border being the Separatrix (last closed flux surface, LCFS). Outside the Separatrix is the Scrape-off layer where the particles are guided directly onto the Divertor plates. As we can see the cross section is not circular but elongated by additional poloidal field coils.

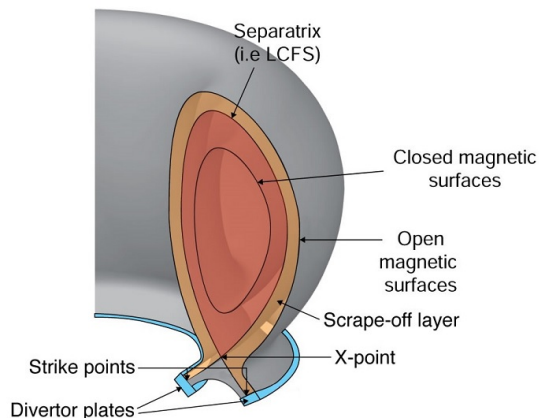


Figure 3: Poloidal cross section of a Tokamak plasma [7].

1.3 H-Mode and Edge Localized Modes

The energy flux through the separatrix is given by

$$P_{sep} = P_{tot} - \frac{dW}{dt} - P_{rad}(core), \quad (8)$$

where P_{tot} is the total heating power, W the total energy stored in the plasma and $P_{rad}(core)$ the radiated power from inside the LCFS. If it exceeds a certain threshold the discharge changes from L-mode (low confinement) to H-mode (high confinement) with the confinement time increasing by a factor of 2. The latter one is characterized by steep edge pressure gradients due to the build up of an edge transport barrier and the occurrence of a pedestal. Figure 4 shows typical pressure profile shapes of L- and H-mode. H-mode was discovered by the predecessor of ASDEX Upgrade, called ASDEX, in 1982. An overview of the characteristics and

the understanding of the H-mode after the first 25 years of research can be found in Ref. [8].

Another characteristic of the H-mode is the periodic appearance of edge localized modes (ELMs) during the collapse of the edge transport barrier resulting in high energy and particle fluxes towards the wall. According to the most accepted theory of ELMs, the so-called peeling-ballooning theory, a complex interplay between sharp edge pressure gradients and large currents in the pedestal drives various MHD instabilities that eventually lead to an ELM [9]. After an ELM, the edge transport barrier builds up again and the edge pressure profiles recover until the next ELM occurs.

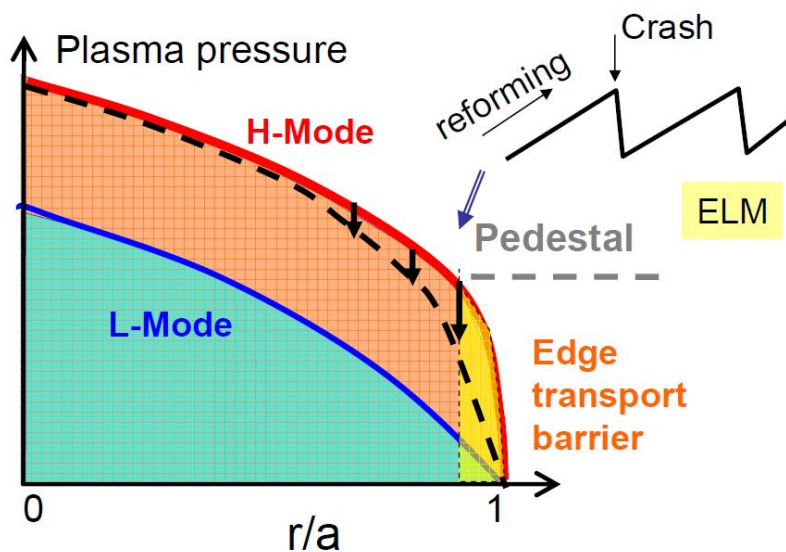


Figure 4: In blue we see a typical L-mode pressure profile. The typical H-mode pressure profiles shown in red are elevated but have the same shape, as if the former one was put on a pedestal. The dashed line shows a profile shape immediately after an ELM, indicating that only the region outside a certain radius is affected and the mode is actually edge localized [10].

The L-H transition is induced by a certain value of P_{sep} shown in eq. 8. In ELM-free H-mode discharges the density rises, with dW/dt going to zero [11]. Furthermore an accumulation of impurity particles in the core can be observed in many Tokamaks which together with the increasing density leads to a rising $P_{\text{rad}}(\text{core})$. Eventually P_{sep} falls below the threshold value and the back transition to L-mode is initiated. ELMs give a mechanism to flush out particles from the plasma and limit the value of $P_{\text{rad}}(\text{core})$. So although ELMs are instabilities decreasing the plasma confinement, they allow for a stationary H-mode discharge.

The exhaust of particles and energy by ELMs can be a serious threat to wall materials of bigger fusion devices in the future like ITER. Since the energy of an ELM rises with the size of a Tokamak to the power of 3 but the area of the Divertor only to the power of 2 and most of the heat load is directed onto the Divertor, the

problem exacerbates with the size [12]. Currently the understanding of ELMs is an important area of research. There are efforts to either use small ELMs to keep the plasma clean from impurities without damaging wall materials or find control techniques to avoid them completely or mitigate their effects.

Examples of the different approaches to suppress or mitigate ELMs are seeding the plasma with impurities to create a radiating divertor, magnetic triggering through vertical kicks, pace-making of ELMs via pellet injection or the application of external magnetic perturbations. The latter one will be described in this work, for a description of the other methods see Ref. [10].

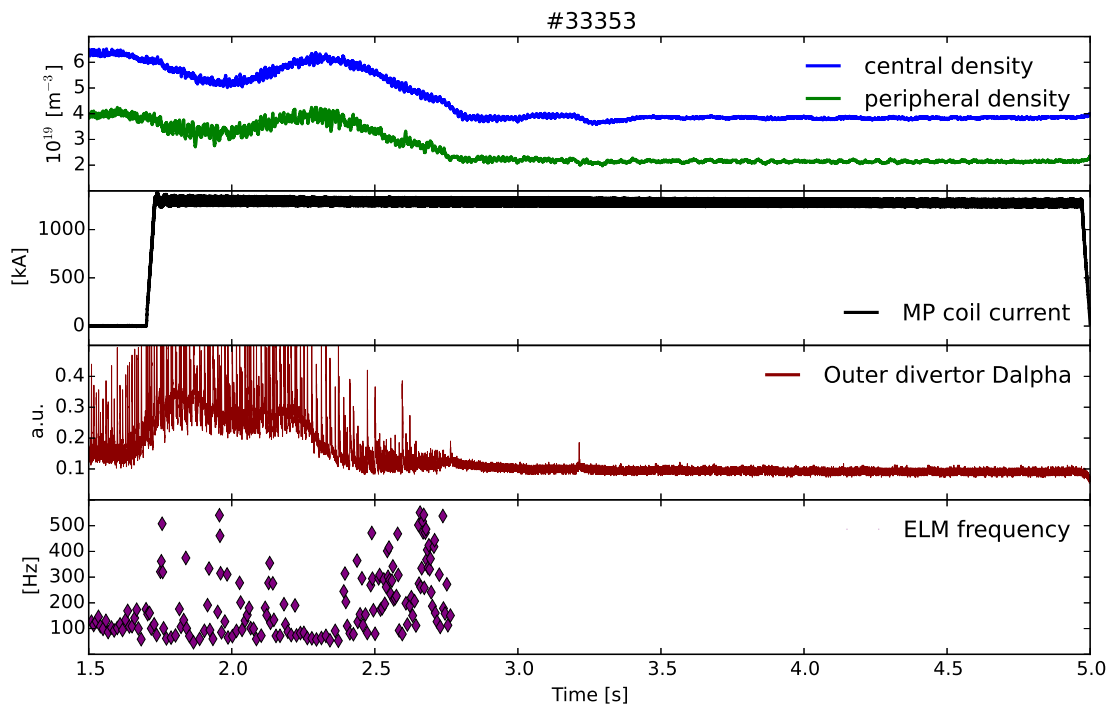


Figure 5: Time traces of ASDEX Upgrade showing ELM suppression. In green and blue, density traces are shown which show a decrease characteristic for MPs, also called density pump-out. In black we see when the current in the perturbation coils is switched on. The D_α line in the outer divertor in red is an indicator of ELM activity, which disappears completely about 1 s after the coils are switched on.

1.4 External Magnetic Perturbations

The original idea behind external magnetic perturbations (MPs) was to create a stochastic layer of the magnetic field in the plasma edge by external coils. This stochastization leads to an increase of the electron thermal diffusivity which decreases the electron pressure gradient to stabilize peeling-ballooning modes. However, some experimental results, for example a decrease of the thermal diffusivity instead of an increase [13], could not be explained with a stochastic layer. Other possible explanations of the increased transport include interaction with turbulent transport and enhanced neoclassical transport [14] or the magnetic flutter model [15].

Regardless of the reason, MPs have showed mitigation and even suppression of ELMs in many different machines. Recently, the complete suppression could also be shown in ASDEX Upgrade [16]. Figure 5 shows time traces of a discharge of ASDEX Upgrade with ELM suppression using the magnetic perturbation coils shown in Fig. 6. The coils will be further explained in chapter 3.2.

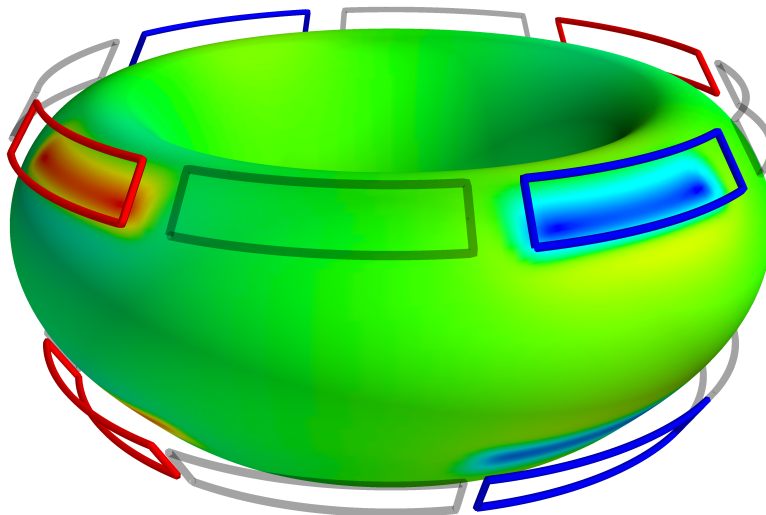


Figure 6: The 16 perturbation coils currently installed at ASDEX Upgrade are arranged in an upper and lower circle to 8 coils each. Red indicates an outwards directed field, blue inwards and green zero corrugation. In green we see a flux surface close to the edge. The plasma response is not considered in this picture, thus it is also called the vacuum field corrugation [17].

1.5 Motivation

For the future use of MPs for ELM suppression it is thought to switch them on before the L-H transition and therefore the behavior of the plasma in L-mode is important to know. Additionally to suppressing ELMs, MPs can cause a significant

distortion of the plasma boundary. Measurements compared with different models found displacements up to 5% of the minor radius in present day machines [18]. These can influence many things, for example the coupling of the ion cyclotron resonance heating or the minimum wall gaps needed for safe operation. Therefore predictions from simulations of the displacement are important for the safety of future machines.

The plasma distortion and stray fields from the perturbation coils can also influence the plasma position control system (PCS, chapter 3.5), which in turn can lead to an exacerbation of the displacement. Investigations in MAST showed the influence of the PCS with an optical plasma edge detection [19]. In this thesis the corrugation and the movement due to the control system will be estimated and compared as follows:

- The corrugation will be measured by density tracing (chapter 4.2) using the lithium beam diagnostic (chapter 3.3) during rigidly rotating perturbations (chapter 4.1).
- The contribution of the control system will be obtained by measuring the plasma corrugation in L-mode with magnetic diagnostics at two toroidally shifted positions (chapter 3.6) as described in chapter 4.3.
- The movement due to the control system will then be subtracted from the perturbed signal of the lithium beam diagnostic, thus maintaining the actual corrugation (chapter 4.4).
- A phase relation between the magnetic flux measured in a poloidal flux probe and the movement due to the control system which could be a hint to stray fields influencing the movement is found (chapter 5.1). An estimation of the corrugation as seen by the control system without the stray fields is also given (chapter 5.2).
- The actual corrugation will then be compared to simulations by VMEC, a code that includes the plasma response to the magnetic perturbations (chapter 2.2) and vacuum field line tracing (chapter 2.3) in chapter 6.

2 Theory and Modeling

2.1 Magnetohydrodynamics

2.1.1 Basics

In comparison to the one particle model and its drift movements (chapter 1.1) a self consistent description of the plasma is needed to answer the questions of equilibrium and stability. This analysis of the macroscopic states of the plasma can be given by the magneto-hydrodynamic (MHD) model. The combination of the fluid equations with Maxwell's equations allows the treatment of macroscopic dynamics of an electrically neutral fluid made up of charged particles. Usually the adiabatic equation (9) is used to close the system of equations of the single-fluid MHD model (10)-(15). It connects the total pressure (electrons and ions) $p=p_e+p_i$ to the ion mass density ρ and can therefore be thought of a kind of compressibility condition. The MHD equations are:

$$p\rho^{-\gamma} = const, \quad \nabla \times \vec{E} = -\frac{\partial \vec{B}}{\partial t}, \quad (9, 10)$$

$$\nabla \cdot \vec{B} = 0, \quad \nabla \times \vec{B} = -\mu_0 \vec{J}, \quad (11, 12)$$

$$\frac{\partial \rho}{\partial t} + \vec{\nabla} \cdot (\rho \vec{v}) = 0, \quad (13)$$

$$\rho \frac{d\vec{v}}{dt} = \vec{J} \times \vec{B} - \nabla p, \quad (14)$$

$$\vec{E} + \vec{v} \times \vec{B} = \eta_{\parallel} \vec{J}, \quad (15)$$

where \vec{J} are the electrical currents in the plasma, \vec{v} the velocity, η_{\parallel} the plasma resistivity parallel to the magnetic field, γ the adiabatic constant, \vec{B} the magnetic and \vec{E} the electric field. (10) is Faraday's law of induction and (11) Gauss' law for magnetism which states the non existence of magnetic mono poles. In Ampère's law (12) the displacement current term is neglected, which eliminates electromagnetic waves from the solutions. This is justified because the dynamic time scales are significantly longer than the time of flight of a photon through the system. (13) is the continuity equation for mass and (14) the force balance equation. (15) is Ohm's law for resistive MHD which turns into Ohm's law for ideal MHD if $\eta = 0$. They are valid for collisional plasmas with $\beta \ll 1$ [2]. Collisional plasma means that enough interactions between the particles are happening to ensure that the system is locally close to thermodynamic equilibrium to treat the plasma as a fluid. For lower collisionality kinetic theory would have to be used.

$$\beta = \frac{p}{B^2/2\mu_0}, \quad (16)$$

which is a measure of the efficiency of confinement, is the ratio between kinetic and magnetic pressure and $\beta \ll 1$ is usually the case for magnetic confined fusion plasmas. Although β gives a value on how efficient a plasma is confined, the Lawson criterion is directly influenced by the total pressure, which can be expressed as $p=2nT$, if all plasma species have the same temperature. Thus Tokamaks and Stellarators still remain the best choice for a fusion reactor since other concepts with lower τ_E must have higher β , which leads to drawbacks concerning stability. Since the conductivity of a plasma is usually very high, ideal MHD gives a good approximation and is sufficient for equilibrium considerations. Resistive MHD is needed to describe the tearing of field lines that can lead to the formation of magnetic islands.

A consequence of ideal MHD is the magnetic flux conservation when moving with the plasma. It is also often described as the magnetic field lines being frozen in the plasma. This means that the topology cannot change as the flux inside small cylinders defined by magnetic field lines would change, if they intersect while following them through the plasma. A proof of this statement can be found in [20]. For changes in the topology the resistive version of Ohm's law is needed.

2.1.2 Equilibrium

An important application comes from the assumption of an equilibrium situation with constant macroscopic quantities $\partial/\partial t = 0$ and zero velocity $\vec{v} = 0$. For this case the force balance is reduced to

$$\nabla p = \vec{J} \times \vec{B}, \quad (17)$$

where the kinetic pressure is balanced by the magnetic pressure. Furthermore all equations but (11) and (12) are eliminated from the system (for the ideal case). By multiplying equation (14) with \vec{J} or \vec{B} we obtain

$$\nabla p \cdot \vec{J} = \nabla p \cdot \vec{B} = 0, \quad (18)$$

which states that the field lines of B and J lie in surfaces with constant pressure. In other words there are surfaces with constant pressure on which the magnetic flux is constant and are therefore also called flux surfaces. The poloidal flux

$$\Psi = \frac{1}{2\pi} \int B_{pol} dS_{\Psi} \quad (19)$$

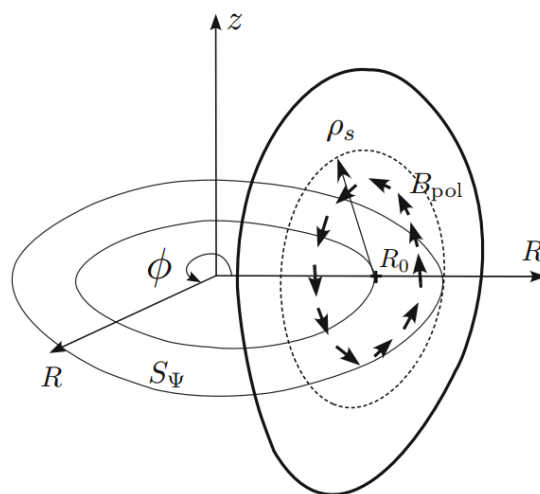


Figure 7: S_{Ψ} is the area and B_{pol} the poloidal magnetic field used for the calculation of the poloidal flux Ψ [10].

is often used and figure 7 shows how the poloidal flux is calculated. The force balance equation can be expressed in terms of the flux function.

$$R \frac{\partial}{\partial R} \left(\frac{1}{R} \frac{\partial \Psi}{\partial R} \right) + \frac{\partial^2 \Psi}{\partial z^2} = -\mu_0 I \frac{\partial I}{\partial \Psi} - \mu_0 R^2 \frac{\partial p}{\partial \Psi} \quad (20)$$

is the Grad Shafranov equation with $I = RB_\phi = I(\Psi)$ being the stream function of the poloidal current. It plays an important role in the axisymmetric equilibrium reconstruction and in general needs to be solved numerically.

With the definition of a flux we can introduce new useful radial coordinates. A commonly used flux coordinate at ASDEX Upgrade is the normalized poloidal flux radius

$$\rho_{pol} = \sqrt{\frac{\Psi - \Psi_a}{\Psi_s - \Psi_a}}, \quad (21)$$

with the index s referring to the separatrix ($\rho_{pol} = 1$) and a to the magnetic axis ($\rho_{pol} = 0$).

2.1.3 Linear Stability

Once a solution for the equilibrium, where the sum of all forces is zero, is found, it is important to know whether it is stable or not. This means if it returns to the equilibrium state after a small initial perturbation or if the perturbation continues to grow. Mechanical analogues are a sphere on a corrugated plane or a pendulum, where the minima of the potential energy are stable equilibria. Equivalent to the potential energy in mechanical systems an MHD expression for plasma systems W can be found and investigated. This is called the energy principle and will be briefly discussed following the derivation in [21]. It uses the approach of linear stability which is often sufficient as it describes well the conditions for excitement or avoidance of instabilities. Another advantage is that it can be treated analytically.

The starting point is the linearisation of the MHD quantities:

$$\vec{B} = \vec{B}_0 + \vec{B}_1, \quad \vec{E} = \vec{E}_0 + \vec{E}_1, \quad p = p_0 + p_1, \quad \vec{v} = \vec{v}_0 + \vec{v}_1, \quad \rho = \rho_0 + \rho_1, \quad (22)$$

where the equilibrium values with index 0 are perturbed by an infinitesimal displacement indicated by the index 1. Furthermore all products of displacement values with index 1 will be neglected. Next the displacement vector $\vec{\xi}$ is introduced, which describes the displacement of a fluid element from the equilibrium position,

$$\vec{v}_1 = \frac{d\vec{\xi}}{dt}. \quad (23)$$

Furthermore all displacement values but the velocity and $\vec{\xi}$ are set to zero for $t = 0$. The linearized MHD equations can now be expressed in terms of $\vec{\xi}$ and integrated over time to obtain the continuity equation (24), the adiabatic equation (25), the combination of Faraday's and Ohm's law (26) and the force equation (27):

$$\rho_1 = -\nabla(\rho_0\vec{\xi}), \quad (24)$$

$$p_1 = -p_0\gamma\nabla\cdot\vec{\xi} - \vec{\xi}\cdot\nabla p_0, \quad (25)$$

$$\vec{B}_1 = \nabla\times(\vec{\xi}\times\vec{B}_0), \quad (26)$$

$$\rho_0\frac{\partial\vec{v}}{\partial t} = \vec{j}_0\times\vec{B}_1 + \vec{j}_1\times\vec{B}_0 - \nabla p_1. \quad (27)$$

The disturbed quantities (index 1) in the force equation (27) can now all be substituted by expressions of $\vec{\xi}$ and a lengthy formula is obtained, which with the MHD-force operator \vec{F} can be written in the form:

$$\rho_0\frac{\partial^2\vec{\xi}}{\partial t^2} = \vec{F}(\vec{\xi}). \quad (28)$$

This in turn allows us to deduce an expression of the change of the potential energy:

$$\delta W = -\frac{1}{2}\int\vec{\xi}\cdot\vec{F}(\vec{\xi})dV. \quad (29)$$

If the change of the potential energy due to a perturbation is negative, the system is unstable, if it is positive, the system is stable. The change of energy can be written in a more intuitive form when the limits of the integral are separated into the space that is occupied by the plasma, the vacuum space and the surface, yielding:

$$\delta W = \delta W_{plasma} + \delta W_{vacuum} + \delta W_{surface}. \quad (30)$$

The contribution of the vacuum is always positive and therefore stabilizing, the surface term will be neglected and the plasma part only contains two terms that can be negative, one proportional to the current and one to the pressure gradient. For details see [21] or other books on MHD [20,22]. This means that there are two basic driving forces of MHD instabilities, the current and the pressure gradient. The term of the pressure gradient is negative, if it points in the same direction as the curvature of the magnetic field line. In a Tokamak this leads to a good curvature side at the high field side and a bad curvature at the low field side that has a destabilizing effect.

To apply the energy principle to a Tokamak, the torus shape is approximated by a cylinder that is bent in a way that the ends connect each other. With this approximation, cylinder coordinates (see fig. 2) can be introduced that are periodical in z and the displacement vector can be expressed in a Fourier series:

$$\vec{\xi}(\vec{x}) = \sum_{m,n}\vec{\xi}_{m,n}(r)e^{-i(m\theta+n\phi)}, \quad (31)$$

where m is the poloidal and n the toroidal mode number. This allows us to classify the instabilities by mode numbers, similar to quantum numbers. An

important term are resonant surfaces where $q=m/n$, which means that magnetic field lines close in on themselves after m poloidal and n toroidal turns. If the displacement there is exactly following the magnetic field lines it is not bending them. Since there is a stabilizing term in δW that is only non-zero when the field lines are bent, instabilities are primarily located on these resonant surfaces.

Note that in an actual Tokamak the field lines don't have a constant pitch due to the inhomogeneity of the toroidal field which can be considered by introducing so-called straight field line coordinates.

2.2 VMEC

Another approach for finding stable plasma equilibria is to solve the problem of the potential energy $dW/dt=0$ by a variational principle. In ideal MHD the total potential energy can be written as

$$W = \int \left(\frac{|B^2|}{2\mu_0} + \frac{p}{\gamma - 1} \right) dV. \quad (32)$$

The Variational Moments Equilibrium Code (VMec) searches for equilibria by minimizing the total potential energy in a three dimensional toroidal geometry [23, 24]. dW/dt can be written as:

$$\frac{dW}{dt} = - \sum_{j,m,n} \int |F_j^{mn}|^2 dV, \quad (33)$$

where F_j^{mn} are the Fourier coefficients representing the forces that have to vanish for an equilibrium state, similar to the force operator in the previous chapter. It assumes nested flux surfaces, calculates their shape and since it uses ideal MHD doesn't allow the formation of magnetic islands or ergodic regions. Furthermore it provides a non-linear solution which means that non-linear coupling of toroidal modes is described correctly. In this thesis the free boundary version is used where the MP-field is incorporated by the continuous pressure boundary condition. Other input parameters are the vacuum field which is generated by all external conductors such as the toroidal, poloidal and perturbation coils, as well as profiles of the pressure, safety factor and plasma current.

Since nested flux surfaces are assumed, the plasma energy (eq.32) can be written in flux coordinates and the geometry of the flux surfaces is described by a Fourier series [23]. This in turn allows us to Fourier analyze the displacement to get the toroidal and poloidal mode numbers. VMec is calculating the R and z components of the displacement, resulting in:

$$\begin{aligned} R(s_i, \Phi, \Theta) &= \sum_{m,n} \bar{R}_{m,n}^c(s_i) \cos(m\Theta + n\Phi) + \bar{R}_{m,n}^s(s_i) \sin(m\Theta + n\Phi), \\ z(s_i, \Phi, \Theta) &= \sum_{m,n} \bar{z}_{m,n}^c(s_i) \cos(m\Theta + n\Phi) + \bar{z}_{m,n}^s(s_i) \sin(m\Theta + n\Phi), \end{aligned} \quad (34)$$

where the index i determines the flux surface, m is the poloidal and n the toroidal mode number. From that we can then calculate ξ_r (eq. 35).

In Figure 8 a poloidal cross section of the poloidal and toroidal corrugation is shown. In blue the actual flux surface is shown, while in black we see the corresponding averaged axisymmetric surface.

$$\vec{\xi}_r = \xi_r \vec{n} \quad (35)$$

gives the definition of the displacement, with \vec{n} being the normal vector of the average axisymmetric surface and the norm that quantifies the local corrugation.

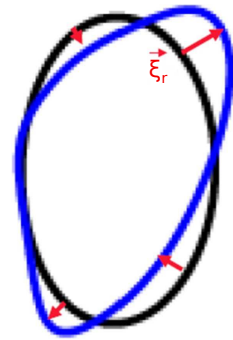


Figure 8: Definition of $\vec{\xi}_N$ [25].

2.3 Vacuum field line tracing

For the vacuum field line tracing the Gourdon code is used to calculate a vacuum field approximation of the magnetic field [26]. As the name already suggests the response of the plasma due to MPs is not considered. The total magnetic field \vec{B} is obtained by adding the vacuum field of the perturbation coils \vec{B}_{MP} to the magnetic field obtained by the axisymmetric equilibrium reconstruction \vec{B}_{EQ} [27]:

$$\vec{B}_{EQ} = -\frac{1}{R} \frac{\partial \Psi}{\partial z} \hat{e}_R + \frac{1}{R} \frac{\partial \Psi}{\partial R} \hat{e}_z + \frac{\mu_0 f}{R} \hat{e}_\Phi, \quad (36)$$

$$\vec{B} = \vec{B}_{EQ} + \vec{B}_{MP}, \quad (37)$$

where Ψ and f are calculated by solving the Grad-Shafranov equation with the CLISTE code, as will be explained in chapter 3.6 and \vec{B}_{MP} by integrating Biot-Savart's law over the current of the perturbation coils surrounded by empty space. The tracing of the vacuum field lines according to:

$$\frac{dR}{d\Phi} = \frac{RB_R}{B_t}, \quad \frac{dz}{d\Phi} = \frac{RB_z}{B_t}, \quad (38)$$

from a certain point in the plasma until it touches the target plate of the Divertor gives us the connection length [28]. Since inside the Separatrix the magnetic field lines are closed, the connection length in this area is usually defined as the distance needed for one poloidal turn, again following the field lines.

A bifurcation occurs when tracing the field lines depending on which direction they are followed. This leads to two connection lengths at every point, the outer manifold is going to the outer target and the inner manifold to the inner target also called stable and unstable manifold.

To estimate the Separatrix position a certain connection length is being tracked from the data obtained by the vacuum field line tracing. Figure 9 shows a plot of the combined connection length at the line of sight of the lithium beam. The connection lengths are combined in a way where always the longer one of the two is taken and then a connection length of 75 m is traced to obtain an estimation of the Separatrix position. We can also think about it like this: If we trace a certain connection length for both manifolds, plot the radial position over Φ and then take the radially outer envelope of these two traces we obtain the same result.

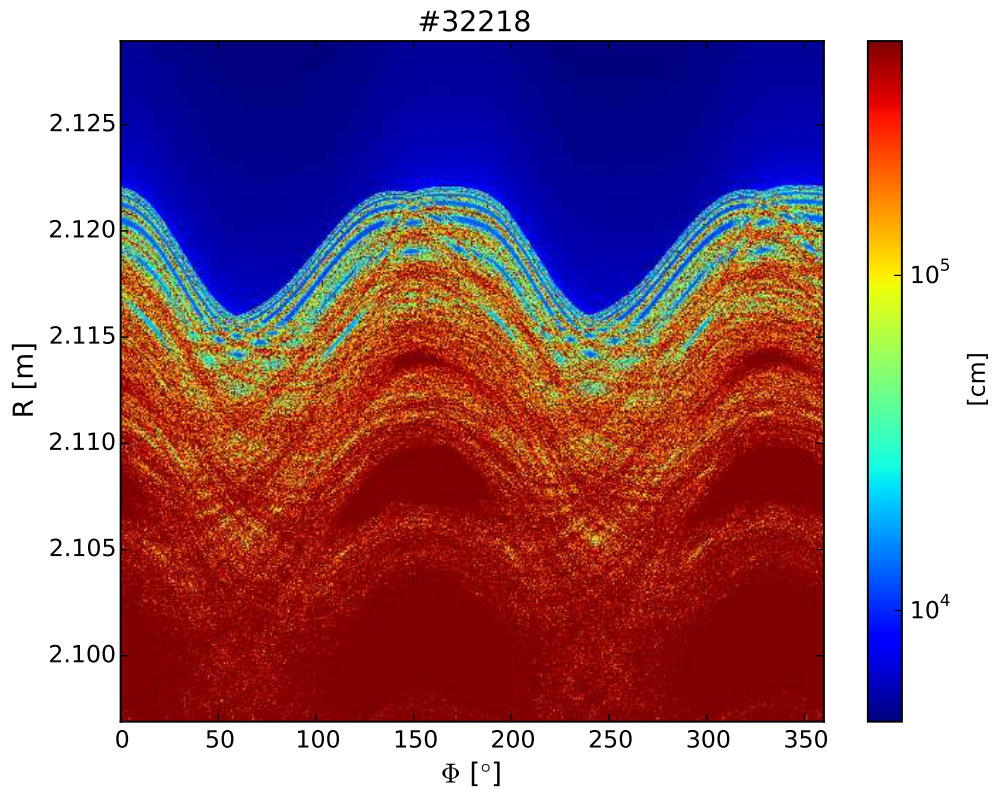


Figure 9: The combined connection length, where the longer length of the two manifolds is taken, at the line of sight of the lithium beam for a whole toroidal rotation for the discharge #32218. The shape of the separatrix can already be seen at the border between the blue and the yellow/green area. Furthermore it can be seen as the outer envelope of two separate sine shapes plotted with a phase difference.

3 Experimental Setup and Diagnostics

3.1 ASDEX Upgrade

The Axisymmetric Divertor Experiment Upgrade, abbreviated ASDEX Upgrade, located at the Max Planck Institute for plasma physics in Garching is a medium sized Tokamak with a major plasma radius of 1.65 m and a minor one of 0.5 m [29]. It is equipped with a heating power of up to 30 MW from various heating systems such as neutral beam injection, electron and ion cyclotron resonance heating and a centrifuge launcher for pellet refueling [30]. The maximum toroidal field created by the 16 toroidal field coils is 3.9 T and the plasma current can reach up to 1.6 MA. The power for the heating and the magnetic system comes from flywheel generators with an installed power of 510 MVA. The length of a discharge is about 10 s due to limitations from the power supply, the heating systems and the thermal load of the coils. The plasma shape is elongated by poloidal field coils located outside the vacuum vessel, as will be needed in a fusion reactor, to allow for the Divertor configuration with an X-point (see chapter 1.2). The design is used for ITER which is constructed as a scaled up version of ASDEX Upgrade, with a similar ratio of heating power to major radius, which translates to a similar heat flux through the plasma boundary.

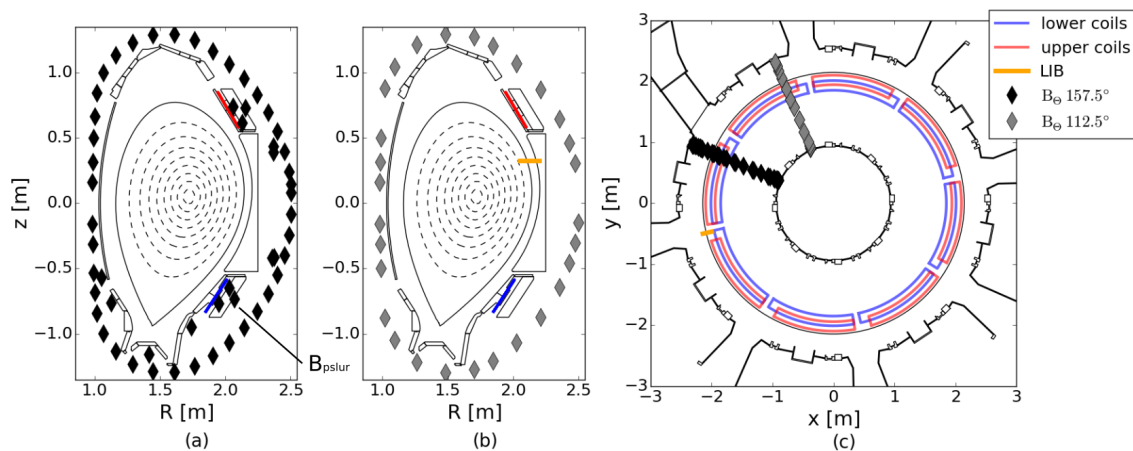


Figure 10: (a) shows a poloidal cut with magnetic probes measuring the poloidal field at a toroidal angle of $\Phi = 157.5^\circ$ in black. The probe B_{pslur} is denoted because of the role it plays later on (chapter 5.1). (b) shows another poloidal cut with the poloidal field probes located at $\Phi = 112.5^\circ$ in grey and the line of sight (LOS) of the lithium beam diagnostic in orange. (c) shows the toroidal position of the probes and the LOS of the lithium beam. In all three pictures the upper round of perturbation coils is shown in red and the lower one in blue.

The scientific goals are the investigation of the ITER baseline scenario including the mitigation of ELMs, exploring advanced Tokamak scenarios, stabilization of instabilities, mitigation of disruptions, optimization of the power exhaust and testing of materials of the first wall. Numerous diagnostics are installed at ASDEX

Upgrade to get information about the plasma parameters, magnetic fields, particle distributions and so on. Figure 10 shows the MP coils, the lithium beam and two toroidally shifted arrays of B_Θ coils, which are used in this thesis and will be explained in the following.

3.2 External Magnetic Perturbation Coils

As already mentioned in chapter 1.4, MPs can play an important role in the suppression and mitigation of ELMs and MP coils are installed in various machines and will also be installed in ITER. Currently there are 16 MP coils installed at ASDEX Upgrade arranged in two circles above and below the midplane (see fig. 6 and 10). They can produce a small non-axisymmetric perturbation in the order of $B_r \sim 10^{-3}B_t$, where B_r is the magnetic field in radial direction and B_t the toroidal magnetic field. 8 more are planned to be installed in the midplane region [31]. 8 coils per row allow for a toroidal mode number n between 0 and 4, two configurations for $n=2$ are shown in figure 11. There has been no effect on ELM behavior for $n=0$ perturbations which indicates the need of a helical structure of the MPs [32]. Another important property is the differential phase angle $\Delta\varphi$ which gives the phase difference of the upper and lower perturbation. It is defined as $\Delta\varphi = \varphi_U - \varphi_L$ where φ_U is the phase of the upper coils and φ_L the phase of the lower ones. $\Delta\varphi$ sets the poloidal mode spectrum depending on q . A crucial dependence of the effectiveness of ELM suppression and mitigation on the differential phase angle between the upper and lower coils has been discovered [33].

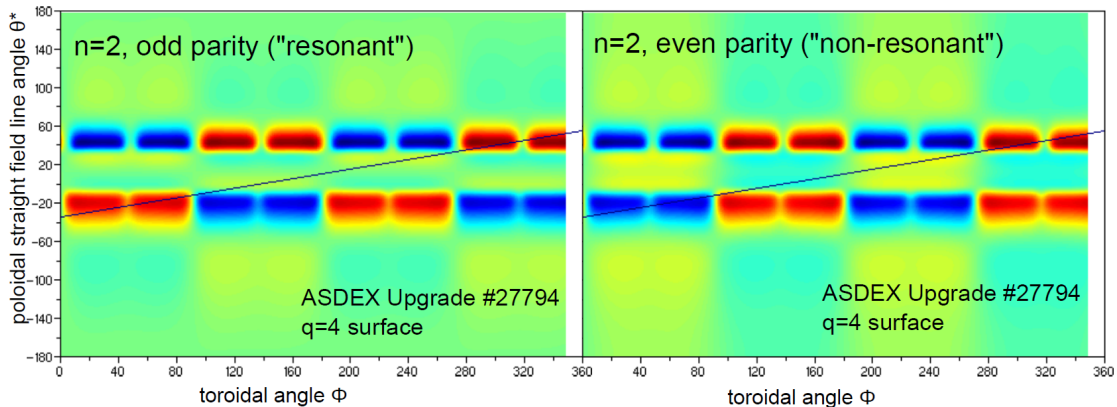


Figure 11: Vacuum field of two different coil configurations using straight field line coordinates, both sides show one flux surface projected on a 2D plane. The color code indicates the radial magnetic field B_r . Green is the unperturbed surface, blue and red indicate deviations in opposite directions. The black line shows a magnetic field line. On the left we see a resonant configuration ($\Delta\varphi = 180^\circ$) since the field line crosses deviations with the same orientation at the upper and lower coils. On the right a non-resonant configuration ($\Delta\varphi = 0^\circ$) with opposite directed deviations is shown [32].

The coils of the MP system are mounted on the two branches of the passive stabilizing loop (PSL, see fig. 13). These two massive toroidal copper conductors are

installed to slow down the vertical plasma movement to make it controllable for the plasma position control, thus providing a kind of damping of instabilities. However they also shield the magnetic field of the MP coils through inducing image currents. To consider this in the simulations the currents in the coils are multiplied by a factor of 0.75 before being used in this work according to finite elements calculations [34].

3.3 The Lithium Beam Diagnostic

The lithium beam works with neutral lithium atoms injected into the plasma in an energy range of 30-80 keV and a beam diameter of about 12 mm. Due to collisions with the plasma particles the single valence electron can be excited from the 2s in the 2p state with subsequent spontaneous or induced de-excitation and the emission of line radiation at $\lambda = 670.8$ nm. The occupation number for the 2p state is dependent on the density and likewise is the intensity of the emitted line radiation. From measuring this radiation we can determine the density of the plasma. The spatial resolution is 5 mm and the temporal resolution used in this work is 1 ms (50 μ s achieved). Figure 12 shows the experimental setup of the lithium beam.

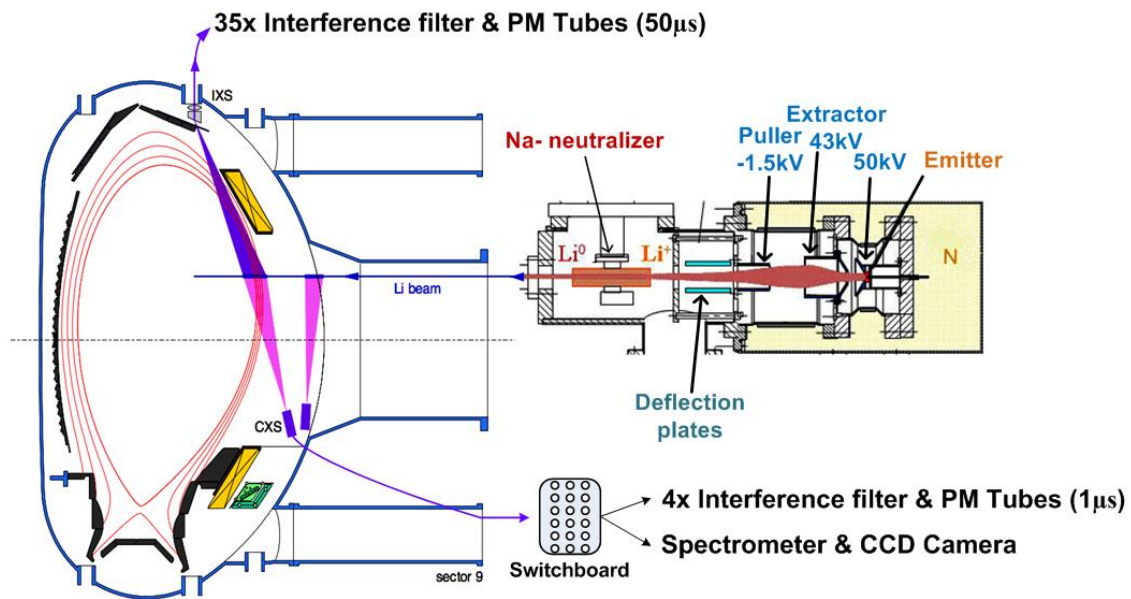


Figure 12: The experimental setup of the lithium beam. On the right we see the injector with the emitter, which is ohmically heated so that ions can be extracted by an applied extraction field, the accelerator, which accelerates and focuses the ions and the Na-neutralizer where the beam is neutralized by a charge exchange reaction with Na. The injector is completely shielded from outside magnetic stray fields which is necessary due to the strong poloidal field of ASDEX Upgrade. On the left we see a poloidal cut of the plasma vessel and the position where the lithium beam enters. The line of sight (LOS) is located at the intersection of the blue area that goes to the upper optical head indicated by IXS (Impact Excitation Spectroscopy) and the blue line which indicates the actual lithium beam. [35].

To calibrate the optical instruments and only consider the radiation of the

lithium atoms, the beam is periodically switched on and off by modulating the extraction voltage [36]. The signal during the switched off phase is averaged and then subtracted from the measured signal when the beam is turned on. One cycle is 80 ms long with the beam being active for 56 ms and shut off for 24 ms.

For a detailed description of the system different kinds of processes are taken into account. These are excitation, induced de-excitation, ionization and charge exchange processes by collisions with plasma particles and spontaneous emission. The emission profiles are then modelled with a system of coupled linear differential equations describing the occupation densities of excited states in Li. This can be expressed as:

$$\frac{dN_i(z)}{dz} = \sum_{j=1}^{N_{Li}} [n_e(z)a_{ij}(T_e(z)) + b_{ij}]N_j(z), \quad (39)$$

$$N_i(z = 0) = \delta_{1i}. \quad (40)$$

The coordinate z goes along the lithium beam with $z = 0$ where the beam enters the plasma. N_i is the occupation density of the energy level i and N_{Li} gives the amount of energy levels considered, in our case 9. a_{ij} is the coefficient that describes population and depopulation rates between different energy levels, ionisation and charge exchange processes (attenuating the Li beam because once ionized they are lost due to the magnetic field). How this coefficient is calculated is for example shown in [37] and [38]. b_{ij} are the Einstein coefficients for spontaneous emission. Finally also the electron density n_e and electron temperature T_e are considered in this equation. Equation 40 is the boundary condition, stating that all lithium atoms are in the ground state when entering the plasma.

To evaluate the electron density from a line emission profile, Bayesian probability theory is used. The probability of an arbitrary chosen density profile under the condition of the measured intensity is given as:

$$P(n_e|d, \sigma, I) = \frac{P(d|n_e, \sigma, I)P(n_e|I)}{P(d|I)}. \quad (41)$$

Then this probability is varied until a maximum is found. The posterior probability distribution function $P(n_e|d, \sigma, I)$ gives the information on how reasonable a solution n_e is, under the requirement that the data d , the uncertainty σ and further information I are given. To calculate it, the prior probability distribution function $P(n_e|I)$, to prevent physically unreasonable solutions or over fitting and the likelihood $P(d|n_e, \sigma, I)$, describing the error statistics of the experiment, are normalized by the evidence $P(d|I)$, which is an important quantity for model comparison. Furthermore positivity and weak monotonicity constraints limit the choice of n_e and allow for smooth profiles. A more detailed description on the probabilistic lithium beam data analysis can be found in Ref. [39].

3.4 B_θ Arrays

Magnetic measurements are based on Faraday's law of induction (eq. 10) with which the magnetic flux ϕ through a surface can be linked to the voltage U induced in a wire coiled around the surface:

$$\phi = - \int_{t_0}^t U(t') dt'. \quad (42)$$

From ϕ the average strength of the magnetic field component perpendicular to the surface can be obtained by $\vec{B} \cdot \vec{n} = \phi / NA$, where \vec{n} is the normal vector of the surface, N the amount of windings around it and A the area of the surface [1]. Therefore the orientation of the coils is important if we only want to determine a certain component of the magnetic field.

There are a lot of differently aligned coils for example for measuring the plasma current or the loop voltage (voltage measured with a toroidal wire loop). For the measurement of the poloidal field, so-called Mirnov coils are positioned to catch the poloidal component of the field. A crucial part is the calibration of the coils with which unwanted interspersals of the toroidal field have to be eliminated. This can be done easily when there is no plasma in the vessel but the toroidal field coils are switched on.

To obtain the flux across the plasma vessel, it has to be extrapolated from the measured fluxes. Due to this the coils have to be positioned as close to the plasma as possible. Here two different arrays of poloidal field coils are used, as shown in figure 10. The plasma control system uses the array located at $\Phi = 157.5^\circ$.

3.5 The Plasma Control System

The performance of the plasma in a Tokamak depends strongly on its shape and position, therefore requiring a control system to keep certain plasma quantities under control and the plasma from touching the wall. Other difficulties can arise from (MHD) instabilities that need to be counteracted, reactions to machine failures and the discharge termination in case of a disruption to avoid stress to the machine's parts. In ASDEX Upgrade the control systems are divided into two parts. The machine control runs continuously and monitors the machine's components. The plasma control is only active during discharges and takes care of various plasma parameters by real-time feedback control of poloidal and toroidal field coils, particle refueling and heating systems on a time-scale of a few milliseconds [40].

One feature of ASDEX Upgrade is that almost all poloidal magnetic field coils are located outside the toroidal field system, as shown in figure 13. Due to the large distance between the coils and the plasma, every coil has a global effect on the plasma and influences all shape quantities. This leads to a non-straightforward handling of shape and position of the plasma also taking into account forces between the coils.

The coils used for the position control are located inside the toroidal field coils as they need a fast response time. The usually controlled values are the vertical position of the current center, also called Zsquad and the radially outermost position of the Separatrix, also called Raus coming from the scalar values of function parametrization (FPP) diagnostic.

The function parametrization is based on a database of several thousand ideal equilibria measurements of mainly poloidal magnetic flux loops, some of the ones shown in figure 10(a). They cover the whole experimentally accessible parameter space of ASDEX Upgrade [41]. Next a principal component analysis is performed obtaining uncorrelated linear combinations of these measurements, omitting linear combinations with small variances and storing the obtained regression coefficients. Up till now these steps are typically only performed once per experimental campaign. For the real-time evaluation the linear combination values are calculated and the quadratic model is evaluated with the previously determined coefficients. This method gives a quick and reliable first estimation of the topology of the equilibrium. However there is no guarantee that the obtained flux is in complete agreement with the equilibrium condition since it is evaluated for every point of the grid separately.

As we can see the plasma control system in ASDEX Upgrade is quite sophisticated and therefore the complex interplay between the control system and the field of the MP coils needs a thorough investigation.

3.6 Integrated Data Equilibrium

A more accurate description of the equilibrium than from the FPP diagnostic can be obtained by the Integrated Data Equilibrium (IDE) diagnostic. It combines an equilibrium solver in the Bayesian framework with kinetic profiles from the Integrated Data Analysis (IDA) concept [42].

The interpretive reconstruction approach of CLISTE uses experimental data from magnetic measurements to solve the Grad-Shafranov equation (eq. 20) numerically. Possibly other diagnostics giving more information about the q profile of the plasma can be added to the evaluation. The numerical approach includes a forward model to iteratively fit the fundamental equilibrium data to the experimental dataset. Values from the FPP equilibrium are used to construct an initial guess and as an input the poloidal field currents and the toroidal magnetic field as well as the magnetic measurements are needed. The differences between the experimental and the modelled measurements are then minimized by a least squares criterion.

However, difficulties with the non-magnetic diagnostics in calibration or avail-

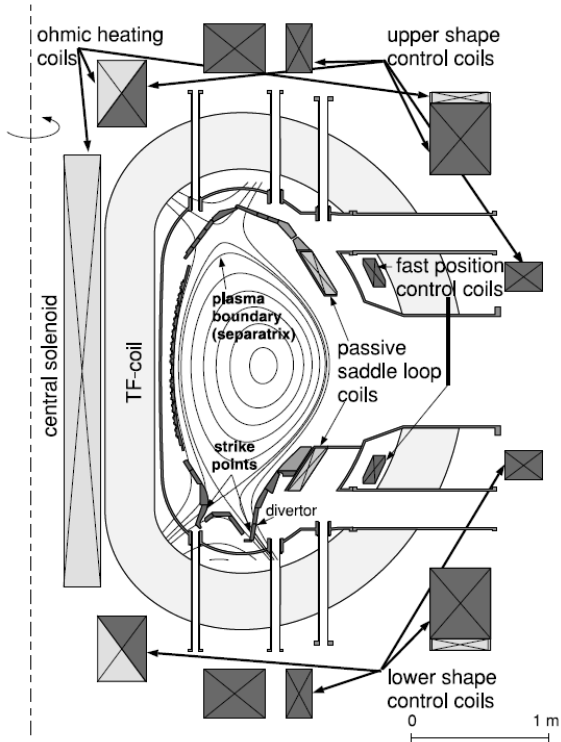


Figure 13: Actuators of the plasma position and shape control system are the ten poloidal field coils as indicated in the picture, also visible are the coils of the PSL [40].

ability can lead to substantial deviations of the obtained current distribution, therefore also the q profile, to the measured ones. Especially in the core plasma the equilibrium can be inaccurate because the magnetic probes are located far from it, as can be seen in figure 13. To improve the equilibrium reconstruction a Grad-Shafranov equation solver is coupled with the results of the current diffusion equation in the equilibrium package IDE [43]. The current diffusion equation gives additional information by modeling the evolution of the current profile which is used for the next equilibrium reconstruction. IDA gives a coherent combination of several plasma diagnostics since the same physical quantities are often measured more than once by different heterogeneous diagnostics [42]. The electron density and temperature as obtained by IDA are then used to solve the current diffusion equation.

4 Method

4.1 Rigid Rotation

A Tokamak is often treated as rotationally symmetric with the poloidal cut being sufficient to describe all necessary parameters. However, with the introduction of the external magnetic perturbations in a helical shape this two-dimensional symmetry is broken. Since diagnostics like the lithium beam are spatially localized and can't be moved, an option is to rotate the MPs. If the differential phase angle $\Delta\varphi$ is kept constant during this rotation it is called a rigid rotation. Furthermore this rotation is the reason of the damping caused by the PSL, since changing magnetic fields induce image currents that weaken the initial field, as already mentioned in chapter 3.2.

Figure 14 illustrates the corrugation of the flux surface in case the plasma response is considered. When the MPs are rotated also the displacement is rotating. This allows us to make two-dimensional measurements with a one-dimensional diagnostic, like the lithium beam is. By measuring over some periods of the rotation we can translate from time to space and get the amplitude of the corrugation. To compare the simulations with the measurements we need to know the toroidal position of the lithium beam Φ_{LIB} , the toroidal mode number n_{tor} , the direction of rotation which gives the sign of n_{tor} , the time-point of the simulations t_0 and the rotation frequency f . The corresponding toroidal coordinate $\Phi_{space}(t)$ of the time dependent measurement of the lithium beam then becomes:

$$\Phi_{space}(t) = \Phi_{LIB} - \frac{2\pi}{n_{tor}} \frac{t - t_0}{f}. \quad (43)$$

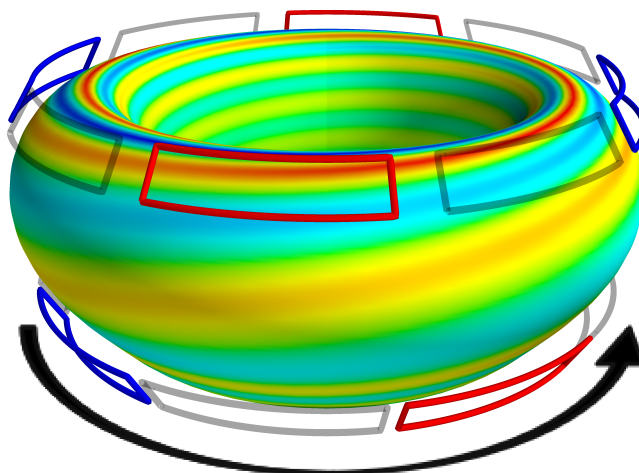


Figure 14: The picture shows a flux surface close to the Separatrix. The perturbation coils are indicated by the rectangles. Red illustrates an outwards directed corrugation, blue inwards and green zero corrugation (see also figure 6). The black curved arrow shows the positive direction of rotation [17].

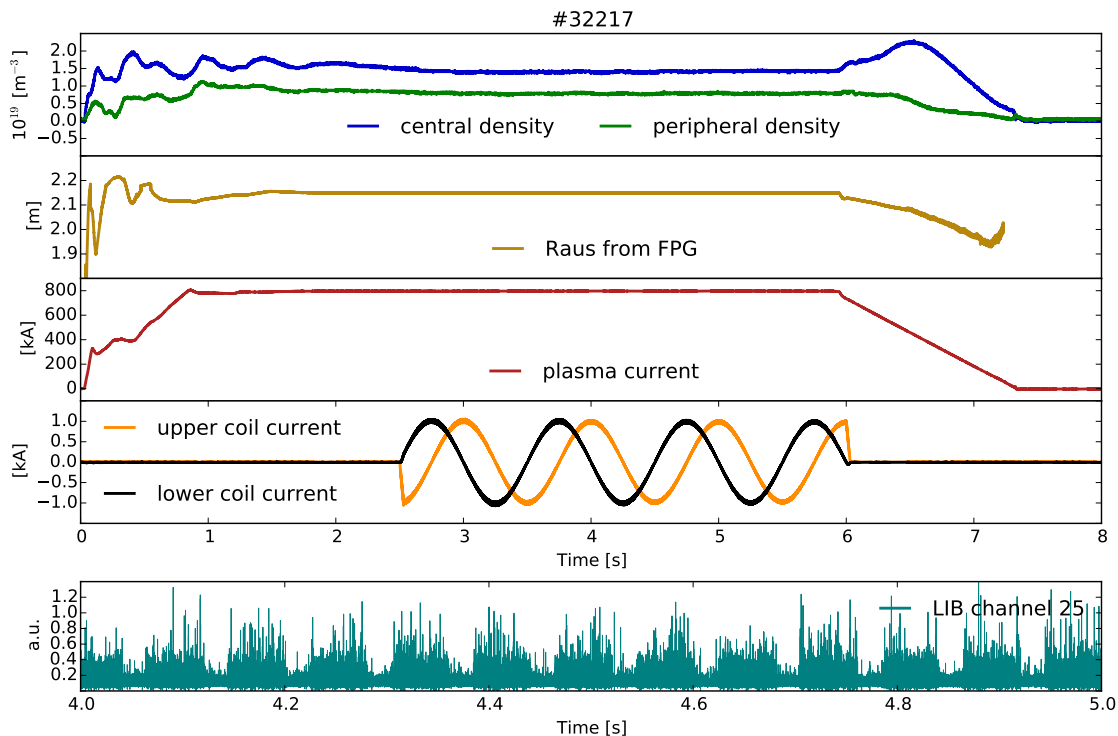


Figure 15: Selected time traces of the discharge #32217. In blue and green we see electron densities from the peripheral and central plasma. Below are the Raus position and the total plasma current as obtained from the FPP diagnostic. In black and orange the currents in a pair of perturbation coils located at the same toroidal position is shown, one in the upper circle and one in the lower one. On the bottom we see the raw signal of one optical channel of the lithium beam. The small gaps in the signal of the lithium beam indicate the periods when the beam is switched off (see chapter 3.3).

A small time delay between the coil currents and the actual perturbation due to the attenuation in the PSL is considered. For the method of rigid rotation it is important to keep the parameters constant during the rotation. Fig. 15 shows selected time traces of an exemplary shot. The perturbation coils are switched on from $t=2.5$ s until 6 s. During this time the density and plasma current are kept constant. The Raus value from FPP is regulated by the position control system and therefore also constant. A 90° phase difference of the upper and lower perturbation coils is seen.

4.2 Measurement of the Displacement

For the measuring of the displacement a diagnostic that is not dependent on the equilibrium reconstruction is needed. Thus the lithium beam was chosen. Figure 16 shows various electron density profiles of the lithium beam measured at three different times. Since the time resolution of the n_e reconstruction is 1 ms and the rotational frequency of the perturbations only 1 Hz several profiles can be chosen close

to the specified time. The first time point at $t \sim 2$ s is before the perturbation coils are switched on. The other two time points at $t \sim 3.3$ s and $t \sim 3.8$ s are half a second apart which translates to half a period and were chosen that the radial shift is the highest from the first profile. The radial shift of the profiles depending on the phase of the perturbation is clearly seen. This in turn allows us to trace the radial position of a certain density. The density values $n_{\text{low}} = 0.3 \cdot 10^{19} \text{ m}^{-3}$, $n_{\text{sep}} = 0.45 \cdot 10^{19} \text{ m}^{-3}$ and $n_{\text{up}} = 0.6 \cdot 10^{19} \text{ m}^{-3}$ were chosen slightly lower than the approximate density of the separatrix before the perturbation coils were switched on at $t = 2$ s. Three values because the mapping of the equilibrium onto the radial coordinate has an uncertainty of about 5 mm and it was later identified as the biggest uncertainty on the evaluation. Slightly lower values because the actual values of the densities don't have a large influence on the evaluation and higher values quickly result in big fitting errors, as will be explained in the following.

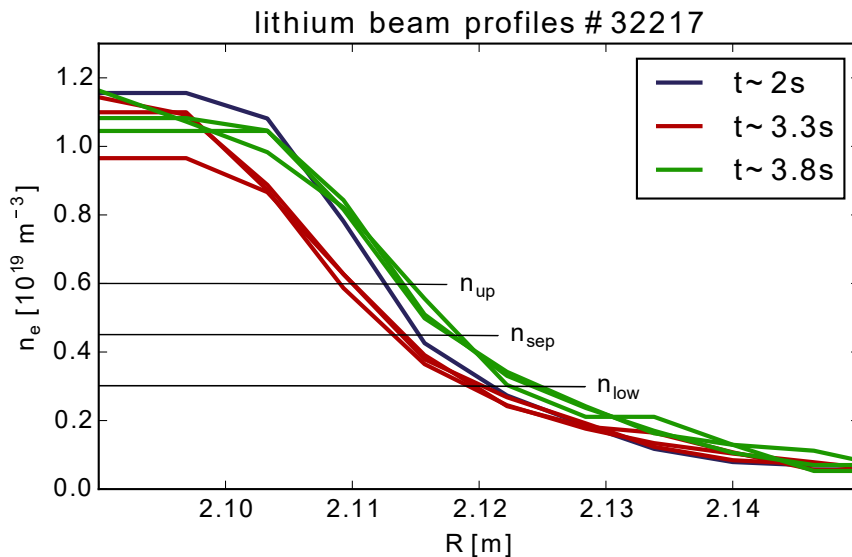


Figure 16: Various electron density profiles from the lithium beam. At $t \sim 2$ s there is no external perturbation applied. Green and red give profiles with a 180° phase difference at the approximate highest deviation from the blue profile.

For the tracing of the Separatrix position two different approaches were tried, the first one was tracing the radial position of the steepest gradient of the profile. First, values above $n_e = 1.75 \cdot 10^{19} \text{ m}^{-3}$ were cut off due to the shape of some profiles where the maximum gradient was located at the radially most inward position. Then a spline interpolation was used to increase the radial resolution. Ultimately the radial position of the steepest gradient was determined. The second approach was to trace a certain density value. The radial resolution was increased by linear interpolation.

The obtained time traces of both methods were then fitted to the function:

$$\xi_{LIB}(t) = \sum_{j=1}^3 |\xi_j^r| \sin(n_{tor} j \omega t + \phi_j) + c, \quad (44)$$

where the first three harmonics are considered. To ensure a better numerical stability during the fitting process the following function was used, instead of eq. 44, for a non-linear least square fit:

$$\xi_{LIB}(t) = \sum_{j=1}^3 A_j \sin(n_{tor} j \omega t) + B_j \cos(n_{tor} j \omega t) + c, \quad (45)$$

where A_j , ϕ_j and c are the parameters to be fitted. The coefficients A_j and B_j can be used for obtaining $|\xi_j^r|$ and ϕ_j with the following relations:

$$\phi_j = \arctan\left(\frac{B_j}{A_j}\right), \quad |\xi_j^r| = \frac{E_j}{\sin(\phi_j)}. \quad (46)$$

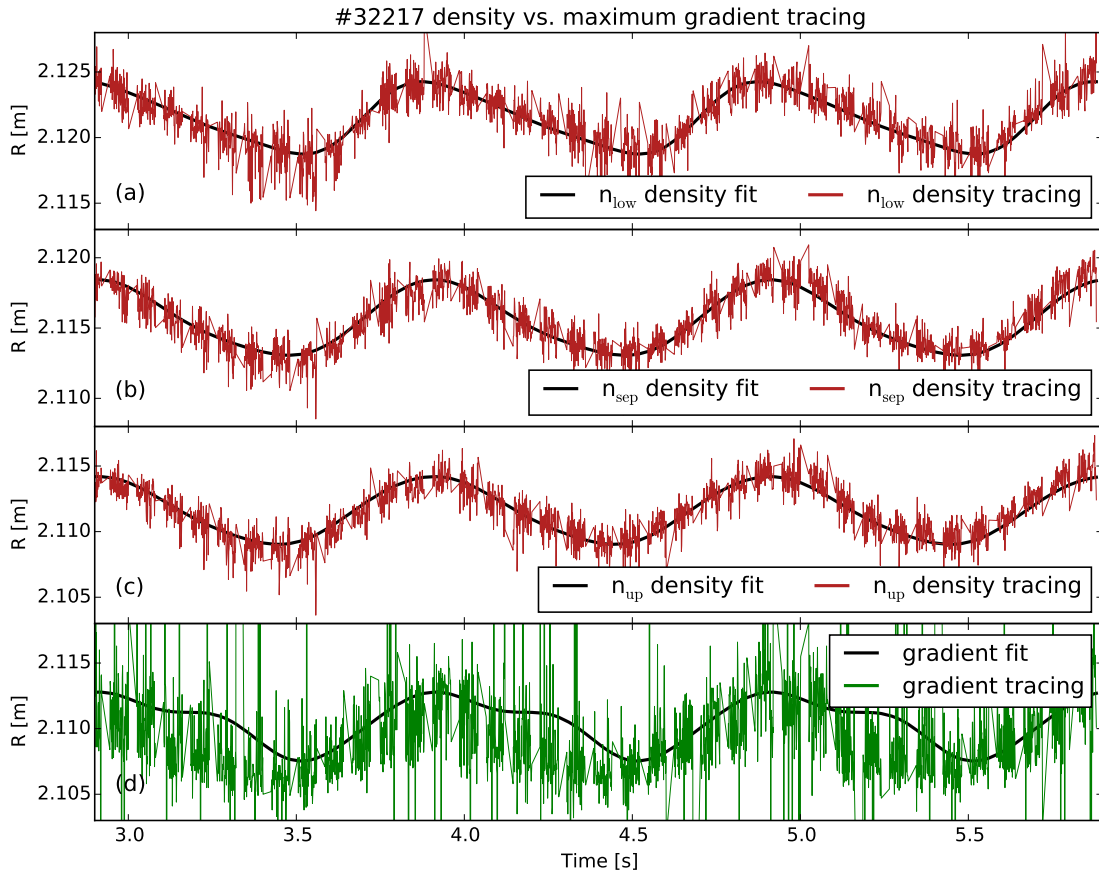


Figure 17: (a), (b) and (c) show the three density traces of n_{low} , n_{sep} and n_{up} which all show a rather good fit. In (d) we see the radial position of the maximum gradient, where the limit of the y-axis is set that some outliers are cut off to ensure a better visibility. The gradient fit shows a distortion due to the consideration of the outliers.

As we see in figure 17 the tracing of the density gives a much better signal than the maximum gradient tracing. Also when removing the outliers that are more than three standard deviations from the signal the density tracing remains the better signal and can be used without smoothing. For higher densities the signal also shows

more outliers, thus the density tracing with the three afore mentioned density values will be used from now on.

A problem with the plasma position control system is that it assumes a two-dimensional geometry using the magnetic probes located at $\Phi = 157, 5^\circ$. This means that the corrugation of the plasma surface will likely result in some kind of reaction of the control system that shifts the whole plasma with an periodic axisymmetric $n=0$ movement. Therefore we also have to consider this movement if we want to obtain the actual corrugation caused by the perturbation coils. The signal of the density tracing then becomes:

$$\xi^{LIB}(t) = |\xi_j^{CL}| \sin(n_{tor} j \omega t + \phi_j^{CL}) + |\xi_j^r| \sin(n_{tor} j \omega t + \phi_j^r) + c_{LIB}, \quad (47)$$

with $j=1,2,3$, the index CL denoting the contribution of the control system (control loop) and r indicating that the displacement is radial. Later on the angle between the line of sight of the lithium beam and the normal vector of the separatrix will be taken into account when the measurements are compared to the simulations since they give the normal vector to the flux surface. It will lead to a change of the amplitude of the actual corrugation of less than 4%. For now, all considerations will be done in the line of sight of the lithium beam.

Since two sine functions with the same frequency that are added can be rewritten to a single sine function with a different amplitude and phase, as in the Fourier series, we cannot distinguish them and get both movements out of one signal. Therefore the movement due to the control system must be obtained from other diagnostics and can subsequently be subtracted from the LIB density trace to obtain the actual corrugation.

4.3 Estimation of the Axisymmetric Movement

To attain the contribution of the control system, equilibria reconstructed by IDE, using magnetic measurements from two toroidally shifted arrays of Mirnov coils were used (see chapter 3.4). It is assumed that both IDE equilibria see the same corrugation amplitude with a different phase. The IDE shotfiles contain the poloidal flux Ψ values on an R-z-grid and the poloidal flux of the separatrix and magnetic axis from which we can calculate ρ_{pol} using eq. 21. Since we want the ρ_{pol} values of the line of sight of the lithium beam, cubic spline interpolation is used to interpolate in between the grid. After that, the separatrix position ($\rho_{pol} = 1$) at the line of sight of the lithium beam as obtained by IDE can be traced.

The locations of the arrays of magnetic loops can be seen in figure 10 with their toroidal angles being $\Phi_{arr1} = 112.5^\circ$ and $\Phi_{arr2} = 157.5^\circ$. That means that they are shifted by 45° which translates to a phase shift in the signals of the rotated perturbation of $n_{tor} \cdot 45^\circ$. Since the movement due to the plasma control system is axisymmetric, it has the same phase in both signals. From now on the radial movement is measured against the mean value of the position of the separatrix during the observed time window, to allow for easier graphical comparison between the discharges. This allows us to omit the constants in the following equations. Therefore, the separatrix traces can be expressed as:

$$\xi^{Arr1}(t) = |\xi_j^{CL}| \sin(n_{tor} j \omega t + \Phi_j^{CL}) + |\xi_j^{EQ}| \sin(n_{tor} j \omega t + \Phi_j^{EQ}), \quad (48)$$

$$\xi^{Arr2}(t) = |\xi_j^{CL}| \sin(n_{tor} j \omega t + \Phi_j^{CL}) + |\xi_j^{EQ}| \sin\left(n_{tor} j \omega t + \Phi_j^{EQ} - \frac{n_{tor}\pi}{4}\right), \quad (49)$$

where EQ denotes the corrugation as obtained by the equilibrium reconstruction. A negative direction of rotation of the perturbation is considered by a negative toroidal mode number.

Now we can subtract eq. 48 from eq. 49 to eliminate the CL term and obtain the EQ parameters in a non-linear least square fit to the corresponding data (Arr2-Arr1). With the EQ parameters the movements can be directly fitted to the data and the amplitude and phase of the control system movement can be acquired.

Figure 18 shows the fits to the separatrix tracing, the movements of the control system and the corrugation as obtained by the equilibrium reconstruction.

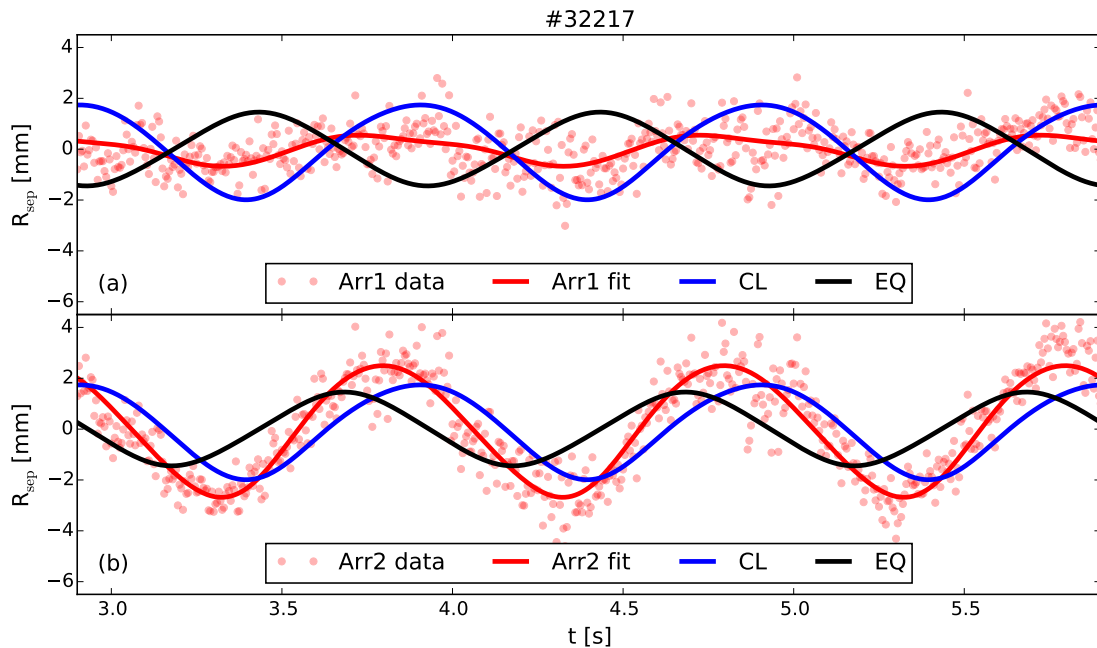


Figure 18: The data points give the position of the separatrix ($\rho_{pol} = 1$) as obtained by the IDE equilibrium reconstruction from (a) array 1 and (b) array 2 for the shot #32217 with $n=2$ and $f=1$ Hz. The corresponding fits are shown in red. The movement due to the control system, denoted by CL, has the same phase at both arrays. The movement of the corrugation has a phase shift of $n_{tor}\pi/4$ which translates to 90° for this shot. We also see that the EQ movement is 90° or 0.25 seconds ahead in time for Arr1 (at $\Phi = 112.5^\circ$) compared to Arr2 ($\Phi = 157.5^\circ$) which is in accordance with the positive direction of rotation for this discharge.

After obtaining the movement due to the control system we can now fit eq. 47 to the density traces of the lithium beam and get the actual corrugation. The uncertainties for the CL, EQ and r parameters were calculated with error propagation

from the uncertainties obtained from the covariance matrix of the fitting routine. However, their values were only in the range of 10^{-5} mm and will therefore not be denoted.

As it turned out the highest uncertainty comes from choosing the value of n_e for the density tracing of the lithium beam. For this reason three densities were chosen and traced (see fig. 16). For each density the parameters of the actual corrugation were calculated individually and the uncertainty given in the following is the standard deviation of the three values.

A change of the densities, for example to $n_{e1}=0.6e19$, $n_{e2} = 0.8e19$, $n_{e3} = 1.0e19$ for #32415 barely changes the shape and phase of R and has only little influence on the amplitudes. The total amplitude for all 3 harmonics changes from $(\max(\xi_r) - \min(\xi_r))/2 = 1.13$ mm for higher densities to 1.24 mm for lower densities and the amplitude of the $n_{\text{tor}}=2$ harmonic is $|\xi_{n=2}^r| = 1.1 \pm 0.2$ mm for both cases.

4.4 Consistency of Method

To determine the consistency of the method we investigate shots with rigid rotation into opposite directions and with reduced current in the perturbation coils and compare the results.

Figure 19 shows the time traces of the plasma discharge #32217. It is a low density L-mode discharge with $n_{\text{tor}}=2$. The amplitude of the $n=2$ harmonic of the actual corrugation becomes $|\xi_{n=2}^r| = 0.9 \pm 0.2$ mm and the total amplitude for all 3 harmonics 1.2 ± 0.2 mm. We can now compare this shot to a discharge with similar parameters but the perturbation is rotated in the opposite direction. This discharge with $n_{\text{tor}}=-2$ and the shot number #32461 is shown in figure 20. In this case the $n=2$ amplitude is $|\xi_{n=2}^r| = 1.5 \pm 0.4$ mm and the total amplitude of all 3 harmonics added up 1.6 ± 0.5 mm. We see a good agreement in the $n=2$ amplitudes almost in the uncertainty range and agreement within the uncertainty range for the total amplitudes of all 3 harmonics. Also the $n_{\text{tor}}=2$ CL and EQ amplitudes show similar values with 1.8 vs 2.1 mm and 1.4 vs 1.6 mm.

Another comparison can be made for the shot #32416 shown in figure 21. It has the same parameters as #32217, only the current in the perturbation coils is reduced by the factor of $\sqrt{2}$ from 1 kA to ~ 700 A. We see that this affects the amplitude of the $n=2$ corrugation $|\xi_{n=2}^r| = 0.4 \pm 0.2$ mm as well as the total amplitude $|\xi_{\text{tot}}^r| = 0.6 \pm 0.1$ mm by reducing them compared to the other discharges. In addition we see the amplitude of the CL movement to be $|\xi_{n=2}^{CL}| = 2.1$ mm and the EQ amplitude also reduces to $|\xi_{n=2}^{EQ}| = 0.8$ mm.

In this chapter we saw the complete method that was used to obtain the actual corrugation. Although the size of the results are on the edge of the sensitivity of the used diagnostics, the three exemplary shots show good agreement with the expected results. For example the corrugation of array 2 located at $\phi = 157.5^\circ$ and the lithium beam at $\phi = 191^\circ$ show a corresponding phase shift. Also the amplitudes of the corrugations show anticipated behavior.

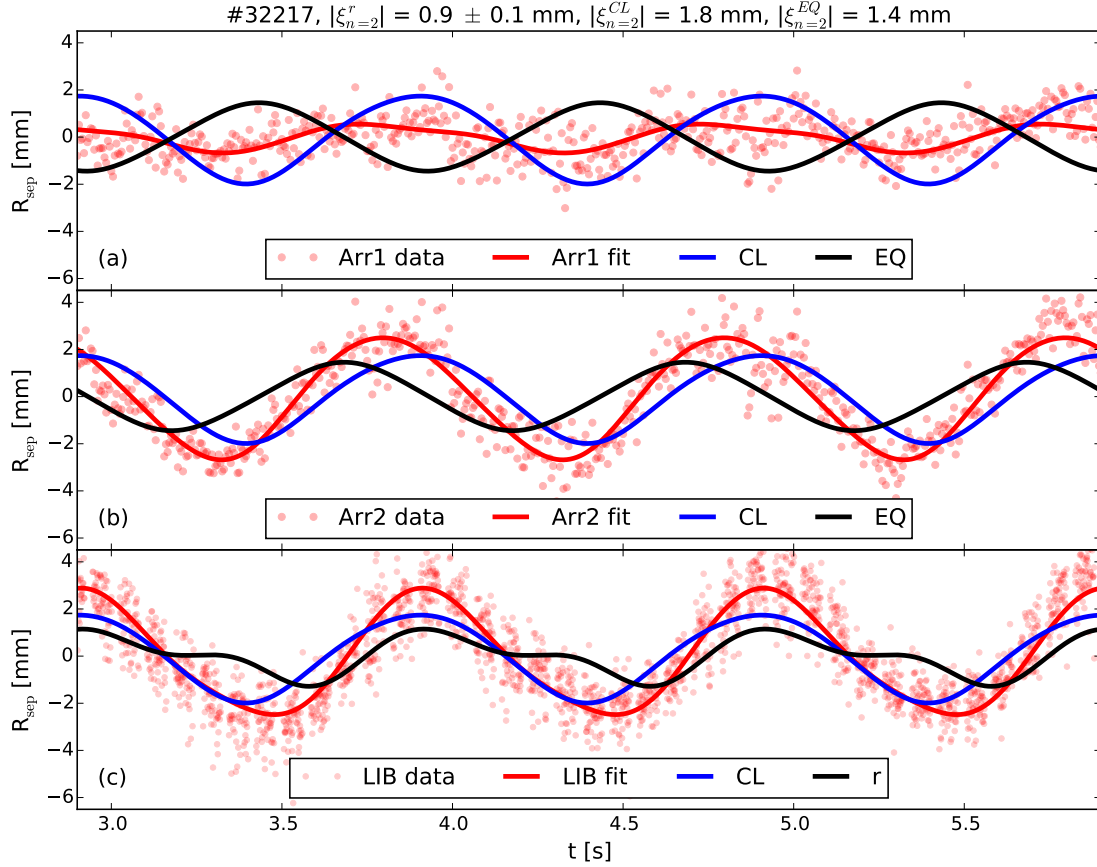


Figure 19: The time traces from (a) array 1, (b) array 2 and (c) lithium beam, where the corrugation as measured by the lithium beam is denoted by r , of the low density L-mode discharge #32217 with a toroidal mode number of 2. We see that the movement due to the control system has the same phase at all three toroidal positions. The EQ corrugation has a phase shift of 90° between array 1 and array 2 and an almost similar phase shift can be seen between array 2 and the lithium beam. Only the shape of the corrugation changes. For array 1 we furthermore see that the CL movement and the corrugation almost cancel each other out through destructive interference.

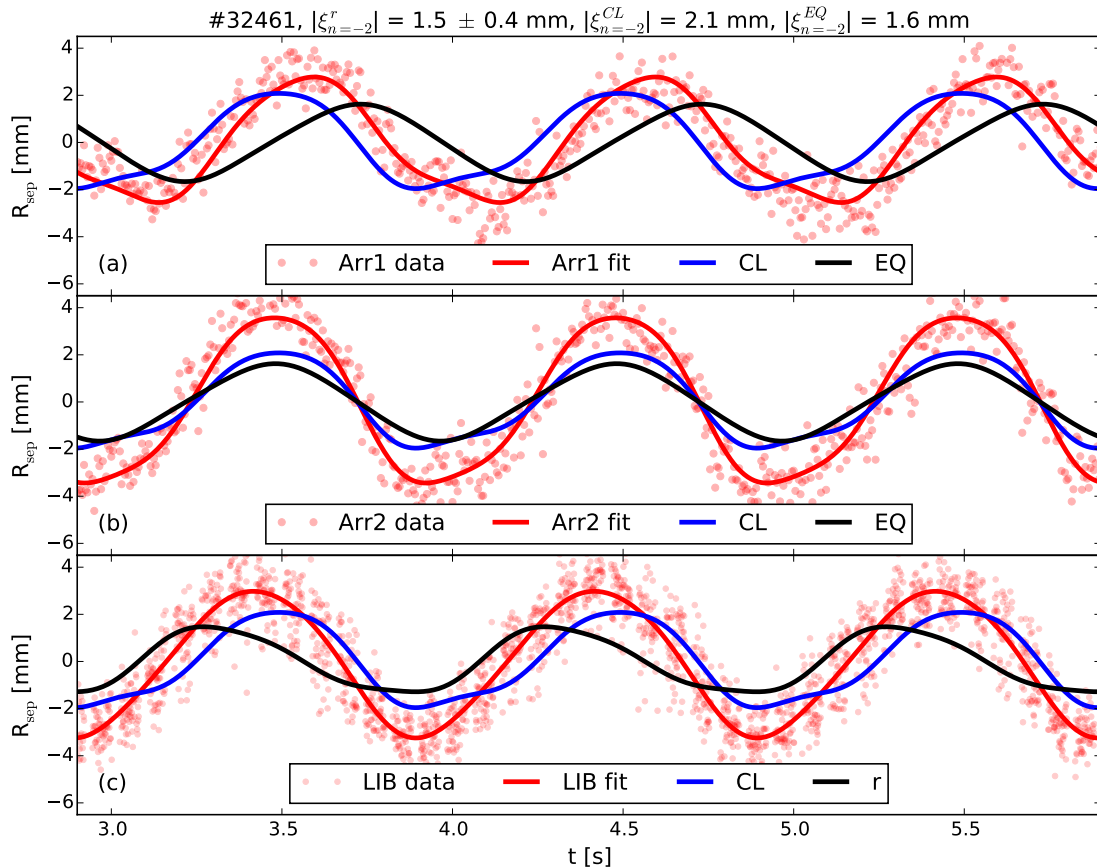


Figure 20: The time traces of the low density L-mode discharge #32461 with a toroidal mode number of -2 from (a) array 1, (b) array 2 and (c) the lithium beam. The phase differences of the EQ and r corrugations is in the opposite direction than for #32217. This is due to the negative direction of rotation.

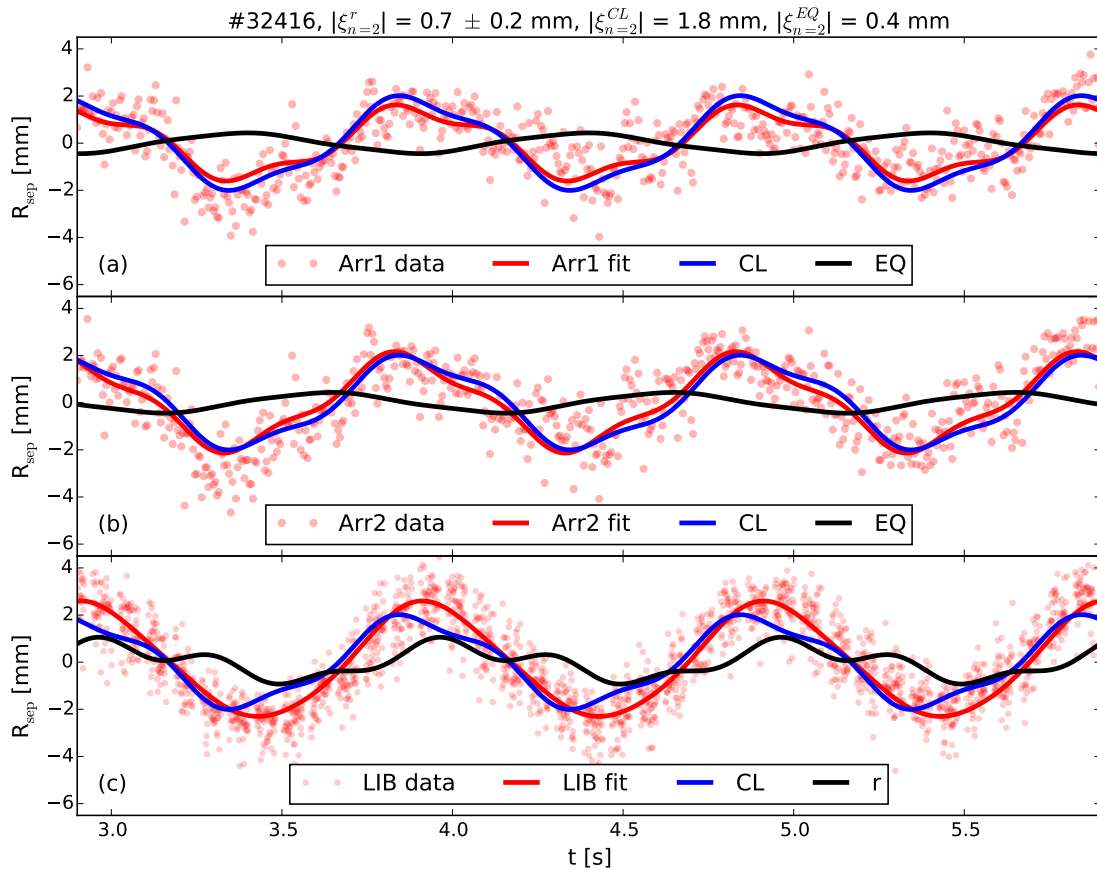


Figure 21: The time traces from (a) array 1, (b) array 2 and (c) the lithium beam of the low density L-mode discharge #32416 with a toroidal mode number of 2 and a reduced current in the perturbation coils. For array 1 the movement due to the control system has the opposite phase of the EQ corrugation. The actual corrugation also shows strong $n=4$ and $n=6$ harmonics.

shotnumber	n	$\Delta\Phi$ [°]	$n_{e,c}$ [10^{19} m^{-3}]	$n_{e,p}$ [10^{19} m^{-3}]	comment
#32217	2	-90	1.4	0.8	pitch-resonant
#32218	2	+90	1.5	0.7	non-resonant
#32219	2		1.4	0.8	upper coils only
#32220	2		1.4	0.8	lower coils only
#32406	2	-90	2.8	1.4	medium density
#32415	2	-90	3.4	1.7	high density
#32416	2	-90	1.4	0.9	reduced current
#32461	-2	-90	1.4	0.8	opposite direction of rotation
#33080	1	-45	1.3	0.7	rotating locked mode
#33189	1	-45	1.2	0.7	reduced current, without mode
#33082	3	-180	1.2	0.7	

Table 1: The shotnumbers, toroidal mode numbers n and $\Delta\Phi$ of the discharges analyzed in this thesis. $n_{e,c}$ indicates the central electron density and $n_{e,p}$ the peripheral one.

4.5 Set of Analyzed Discharges

Table 1 shows the discharges analyzed in this thesis. They are all L-mode discharges with different characteristics. A rotation frequency of 1 Hz was applied for all shots. The toroidal mode number n was varied from 1 to 3 with emphasis put on $n=2$. A negative mode number indicates a negative direction of orientation for the rigid rotation, clockwise when seen from above. $\Delta\varphi$ was mostly chosen in a way that the magnetic perturbation aligns with the magnetic field and therefore being resonant. For $n=1$ and $n=3$, $\Delta\varphi$ has to be divided or multiplied by two, to get the same pitch of the MPs as for $n=2$, thus resulting in -45° or -180° respectively. For #32218 it was chosen to be non resonant and for #32219 and #32220 only the upper or lower coils were used, hence $\Delta\varphi$ is not defined for those cases. $n_{e,c}$ and $n_{e,p}$ show the line integrated electron density of two different lines of sight in the plasma. $n_{e,c}$ goes through the central plasma and $n_{e,p}$ through the peripheral plasma, thus giving an indication of either the central or peripheral density. The density values are approximately the ones during the analyzed time window and were mostly rather constant in time. Only for #33080, #33189 and #33082 the densities showed a higher variation over time. We can see that the densities are pretty similar, except for the medium and high density cases. For #32416 the amplitude of the currents in the perturbation coils was reduced by a factor of $\sqrt{2}$ compared to the other $n=2$ cases and for #33189 by the factor of 4 compared to #33080. In all the shots the perturbation coils were switched on in the time from 2.5 - 6.0 s. To give the plasma and the PSL some time to react the analysis was performed from 2.9 s until 5.9 s, only in some cases where the density changed, a shorter time window was chosen to prevent fitting errors due to the density separatrix tracing of the lithium beam.

5 Role of the Plasma Position Control

5.1 Behavior, currents B_{pslur} vs CL

In chapter 4 we have seen that the plasma control system applies a significant movement to the plasma that interferes with the measurement of the corrugation. The amplitudes of these movements can be higher than the amplitude of the corrugation and depending on the phase shift it can amplify or mitigate the measured signals.

Apart from not taking into account the 3-dimensional magnetic geometry induced by the MPs, the control system does not take into account the stray fields from the perturbation coils. For this reason the measured magnetic fields of the poloidal field coils that are used in the FPP diagnostic were checked for periodic modulations. The highest amplitude of a 1 Hz sine modulation was found in the signal of a coil named B_{pslur} , which is located close to the lower PSL and therefore also close to the perturbation coils. This coil is usually not taken into account for the IDE and CLISTE equilibria since measurements with too high residuals are neglected.

Figure 22 shows the time traces of the magnetic field B_{pslur} as measured by the afore-mentioned coil and the movement due to the control system. Both oscillations are having a similar phase angle with the CL movement seeming to be slightly ahead for the most discharges. Only for #32461 it is slightly delayed which could be explained by the direction of rotation, since it is the discharge with $n=-2$. The signals of #33189 both show a small amplitude because the current in the perturbation coils is reduced to 250 A, which is a quarter of the normally used current. The amplitude of the corrugation is significantly reduced to 0.3 ± 0.1 mm due to this. #32219 is not shown because only the upper coils were used for this shot and no modulation was observed in the magnetic field signal. The observed time frames for #32415 and #33080 are shorter because the density was not kept constant in the neglected time windows.

This observation could give a hint that the movement due to the control system is induced or amplified by the stray fields of the perturbation coils.

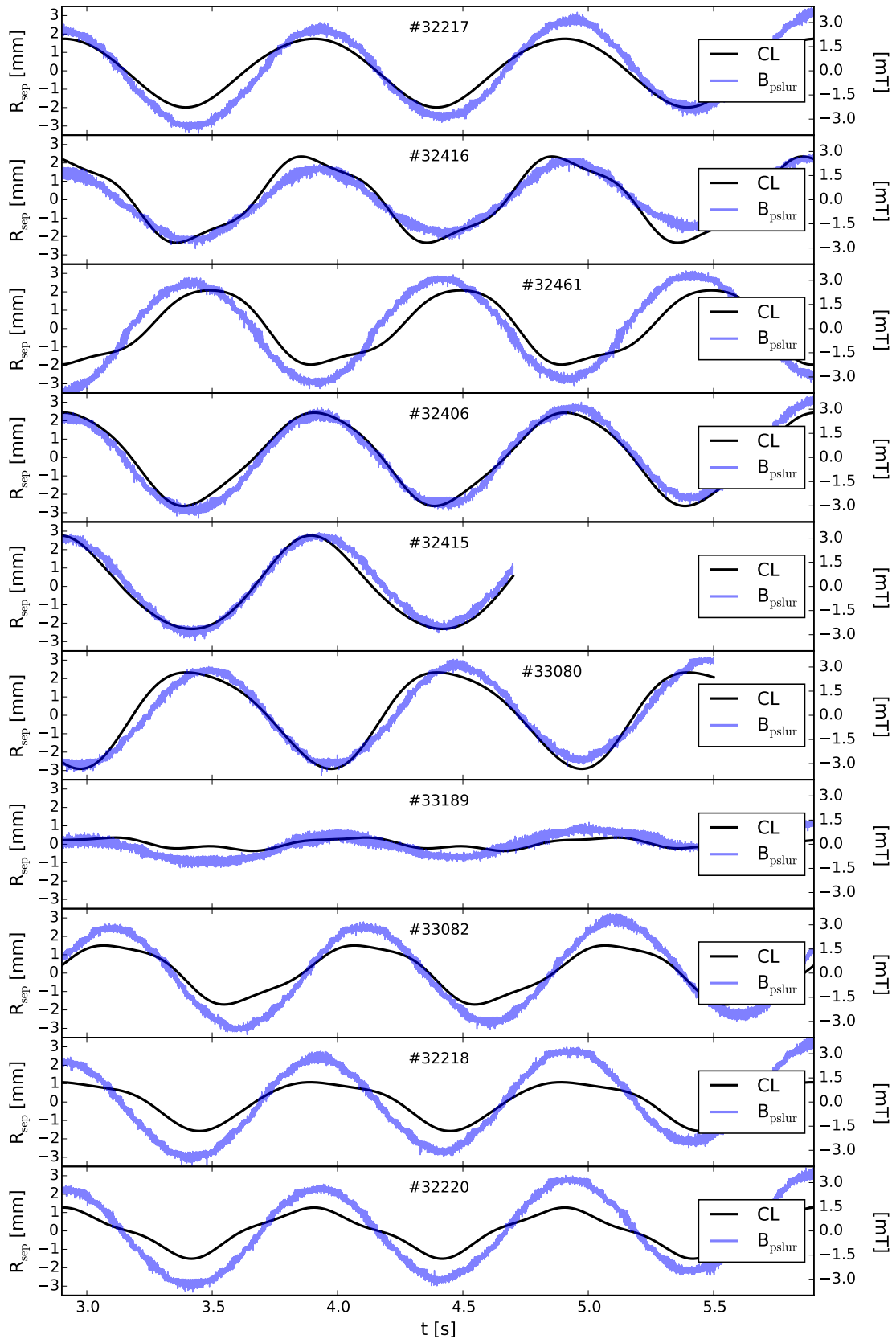


Figure 22: The time traces of the magnetic field B_{pslur} and the movement due to the control system CL for selected discharges.

5.2 Estimation of the 3D Components on the Axisymmetric Equilibrium

An estimation of the corrugation that the plasma control system would see, if the stray fields of the perturbation coils were considered, can be given. To do that two different approaches were tried. For the "2D" case the magnetic field components B_R and B_z were calculated for 64 toroidal positions separately, using VMEC and the MFBE code package [44], assuming toroidal symmetry for each position. For the "3D" case the B_R and B_z were taken from the three-dimensional VMEC simulation. From this we can calculate the poloidal flux (see eq. 19) for both versions. First, integration over z yields the flux at the smallest R of the grid:

$$\Psi_{R_0}(z) = \int_{z_0}^z -2\pi R_0 B_R(R_0, z') dz', \quad (50)$$

where B_r is the radial magnetic field and R_0 and z_0 the smallest R and z of the grid. Subsequently B_z is integrated with respect to r to obtain the poloidal flux Ψ dependent on R and z :

$$\Psi(R, z) = \int_{R_0}^R 2\pi R' B_z(R', z) dR' + \Psi_{R_0}(z). \quad (51)$$

To be able to trace the separatrix, ρ_{pol} (eq. 21) was then calculated, for which the flux on the magnetic axis and the separatrix is needed. Since the X-point is located on the separatrix, the flux at this location can be used. To obtain it the saddle point of the poloidal flux with a maximum on the R -axis and a minimum on the z -axis has to be found. For the flux of the magnetic axis, the maximum of the poloidal flux has to be obtained. With these two values the poloidal flux coordinate ρ_{pol} can be determined. Figure 23 shows a poloidal cut of Ψ with the locations of the X-point and the magnetic axis. The R_{aus} value is then obtained by the maximum R value of the trace of $\rho_{\text{pol}}=1$. To increase the spatial resolution the flux is interpolated between the grid points using cubic spline interpolation during all these steps.

Figure 24 shows the obtained estimations for the 4 principal $n=2$ configurations. The 2D and 3D results were also compared to the movement due to the control system ξ_{CL} and the corrugation ξ_{EQ} but showed no systematic phase

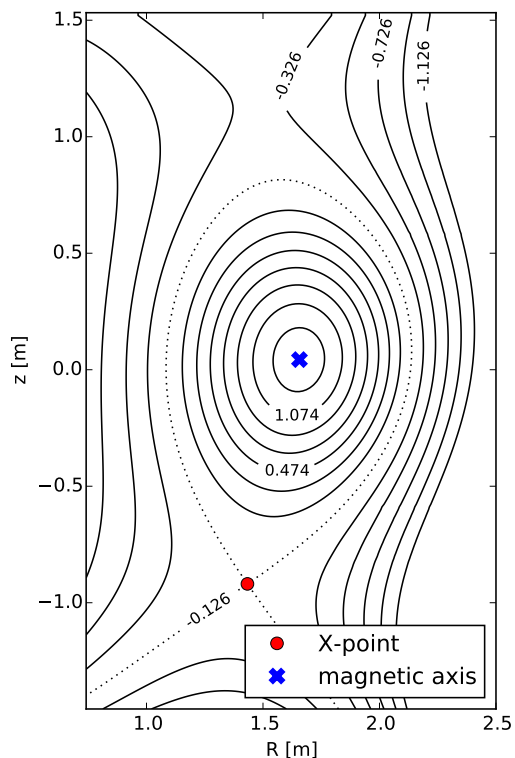


Figure 23: Poloidal cut of the poloidal flux Ψ . The X-point is located at the intersection of the separatrix surface, which is shown in a dotted line.

relations and are therefore not shown. This means that the calculated movement does not reflect the behavior of the control system because stray fields also play an important role. A comparison of the amplitudes shows that $|\xi_{CL}|$ is between the 2D and 3D amplitude, only for #32219 it is lower. $|\xi_{EQ}|$ is lower than the 2D and 3D amplitudes, except for #32217 where it is between them. In general the 2D and 3D amplitudes are higher in comparison to the measured values for the non-resonant configurations than for the resonant one.

The CL movement obtained by the method described in chapter 4 is an overlay of the actual corrugation and the stray fields that are not considered in the FPP diagnostic. Therefore the behavior of the control system at ASDEX Upgrade is different to the one used at MAST by Chapman et al. [19] since they are using an optical system to measure the position of the Separatrix. At AUGD the magnetic system leads to a different behavior of the control system.

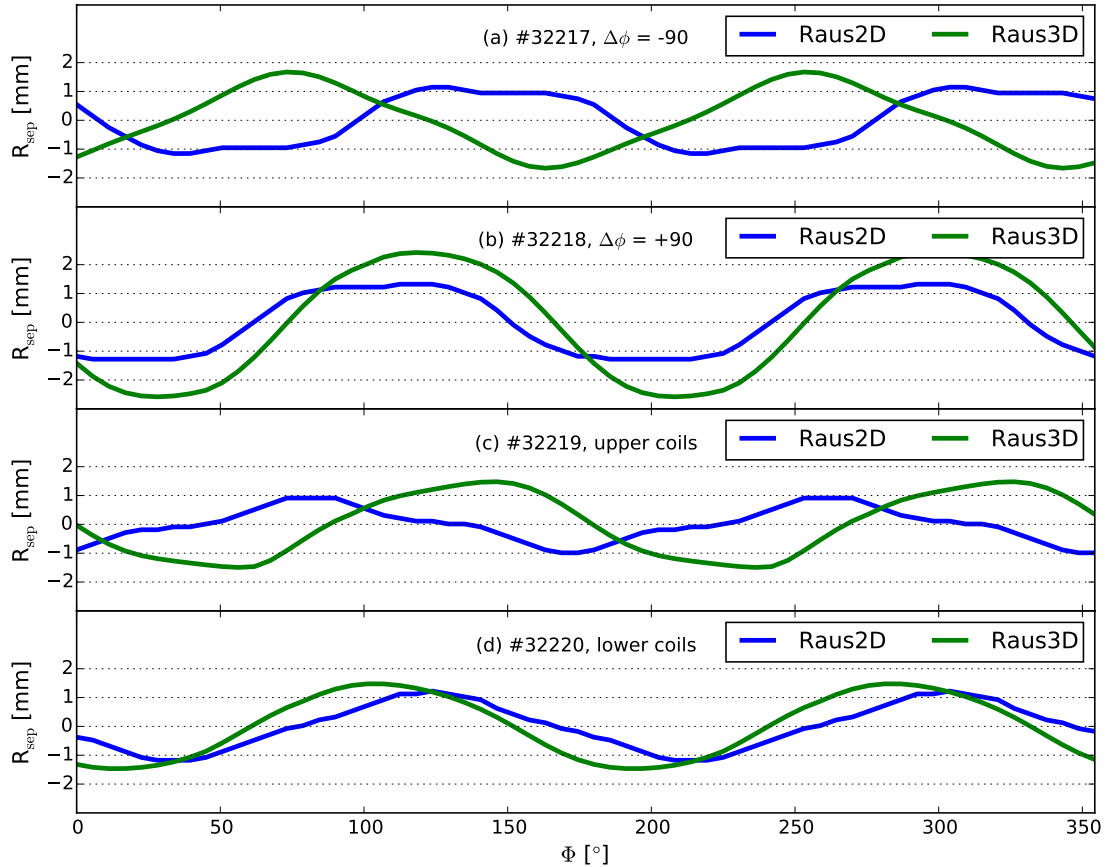


Figure 24: The estimations of the corrugation for the 4 principal $n=2$ configurations versus the toroidal angle Φ . In blue the 2D version and in green the 3D version is shown. (a) The resonant configuration #32217 shows an amplitude of 1.1 mm for the 2D case and 1.7 mm for the 3D. (b) The non-resonant configuration #32218 shows 1.3 mm for 2D and 2.5 mm for 3D. (c) The configuration with only upper coils switched on #32219 gives 1 mm for 2D and 1.5 mm for 3D. (d) The lower coils only configuration #32220 gives 1.2 mm for 2D and 1.5 mm for the 3D case. The amplitudes for the 3D case are higher than for the 2D case for all 4 configurations. No similar phase relations can be observed.

6 Results

To gain knowledge about the predictability from simulations, the results of the method described in chapter 4 are now compared to VMEC and Vacuum field line tracing. For VMEC and the actual corrugation obtained from the measurements the signals can be divided into their harmonics.

6.1 $n=2$ Comparison and Side Bands

For the shots with $n_{\text{tor}}=2$ the amplitudes and phases of the complete signals and their first three harmonics have been compared. Fig. 25 shows the corrugation from the measurement compared with the VMEC simulation of the discharge #32217. The simulation and measurement agree very well for the complete signal and the $n=2$ harmonic. The $n=4$ and $n=6$ harmonics are in less good agreement with the uncertainty being too large to allow for a distinct statement.

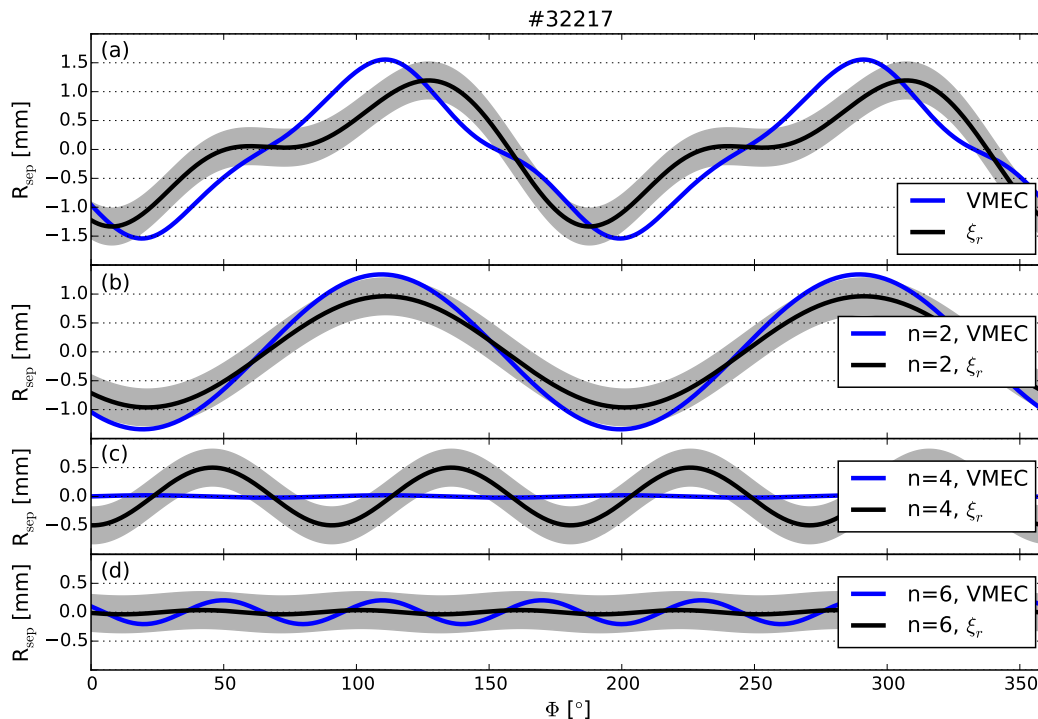


Figure 25: The obtained corrugation and the VMEC simulation of #32217 versus the toroidal coordinate Φ . The measured corrugation $|\xi_r|$ is shown in a shaded area which gives the standard deviation of the amplitude. (a) the amplitudes for the complete signal agree well with 1.2 ± 0.3 mm for the measurement and 1.5 mm for the VMEC simulation. Also the phase shows similar behavior. (b) the phase of the $n=2$ harmonic agrees very well, with the amplitudes yielding 1.0 mm for the measurement versus 1.3 mm for VMEC. (c), (d) the $n=4$ and $n=6$ harmonics show less good agreement with the amplitude of VMEC being almost zero for $n=4$ and the amplitude of the measurement being almost zero for $n=6$ and a large uncertainty range.

The agreement between the VMEC simulation and the measured corrugation for the fundamental oscillation and less good agreement for the higher harmonics and a relatively large uncertainty range is also observed in the other shots that are analyzed.

6.2 $n=2$ Comparison with Different Coil Configurations

In this chapter a comparison between different coil configurations of shots with $n=2$ will be shown. The configurations are resonant and non-resonant, where the non-resonant cases are either with a $\Delta\varphi=+90^\circ$ or only with upper or only lower perturbation coils switched on. The simulations with VMEC have been done using the input equilibrium of #32217 at $t=2$ s before the coils were switched on, for all 4 coil configurations, namely the discharges #32217, #32218, #32219 and #32220.

Figure 26 shows the vacuum field line calculations of the resonant and lower coils only configuration and the position of where the Separatrix was estimated (see also chapter 2.3 and figure 9).

Figure 27 shows the corrugation as obtained from the measurements, VMEC simulations and vacuum field line tracing for all 4 different coil configurations. All discharges show a good agreement between VMEC and the measurement. The vacuum field line tracing shows a better agreement for the non-resonant cases.

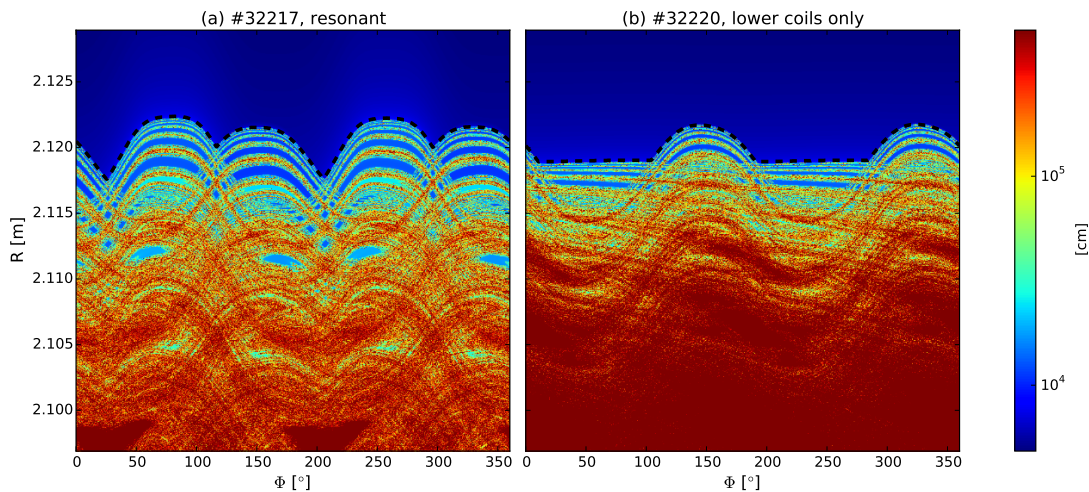


Figure 26: The vacuum field line tracing calculations at the position of the lithium beam for (a) the resonant and (b) the lower coils only case. In dashed black a connection length of 75 m is plotted, which was used as an estimated position for the Separatrix. Higher values for the connection length quickly result in a distorted signal as we see from the plots that the connection length is not continuously increasing in the radially inward direction. In (b) we see that one manifold has no sinusoidal shape. This can be explained because the magnetic field between the position of the lithium beam and the inner target is not perturbed as the upper coils are not switched on.

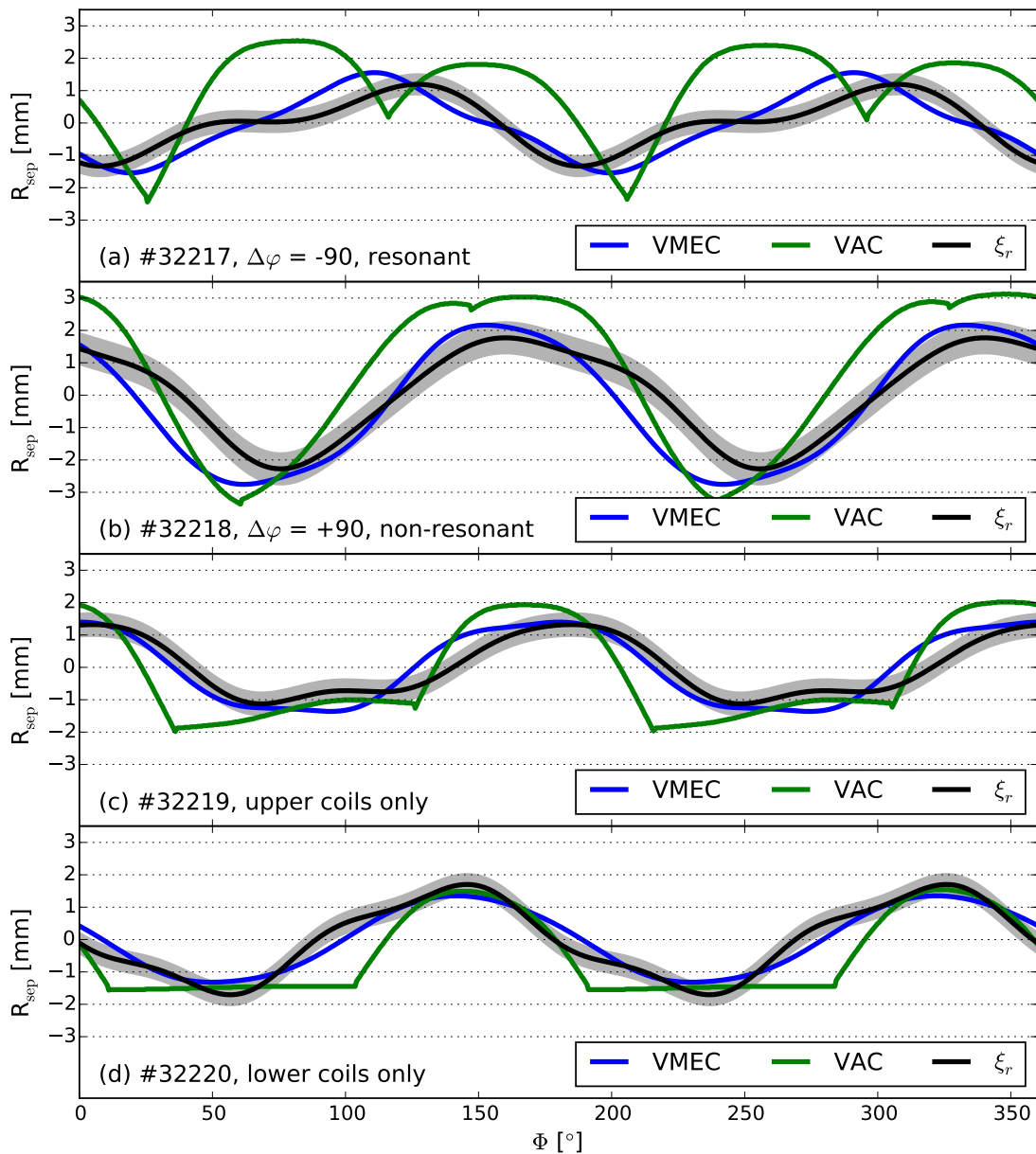


Figure 27: Separatrix positions as obtained from VMEC in blue, vacuum field line tracing in green and measurement in black for different $n=2$ coil configurations versus the toroidal coordinate Φ . (a) shows the resonant case with amplitudes of 1.3 ± 0.3 mm for the measurement, 1.5 mm for VMEC and 2.5 mm for the vacuum field. (b) shows the non-resonant case with both coil circles switched on and amplitudes of 2 ± 0.5 mm for the measurement, 2.5 mm for VMEC and 3.2 mm for the vacuum field. (c) shows the upper coils only case with 1.2 ± 0.4 mm for the measurement, 1.4 mm for VMEC and 2 mm for vacuum field. (d) shows the lower coils only case with amplitudes of 1.7 ± 0.3 mm for the measurement, 1.3 mm for VMEC and 1.5 mm for the vacuum field. For an explanation of the flat parts of the vacuum tracing see figure 26.

6.3 Density Scan

A comparison of the plasma response for different densities is given in this chapter. It is important to know if and how the plasma response to MPs is behaving at different densities to ensure better predictability for future machines. In figure 28 profiles of the lithium beam of the three analyzed shots are seen (compare figure 16). The different densities are clearly observed and at first sight no clear change of the amplitude of the horizontal movement is visible.

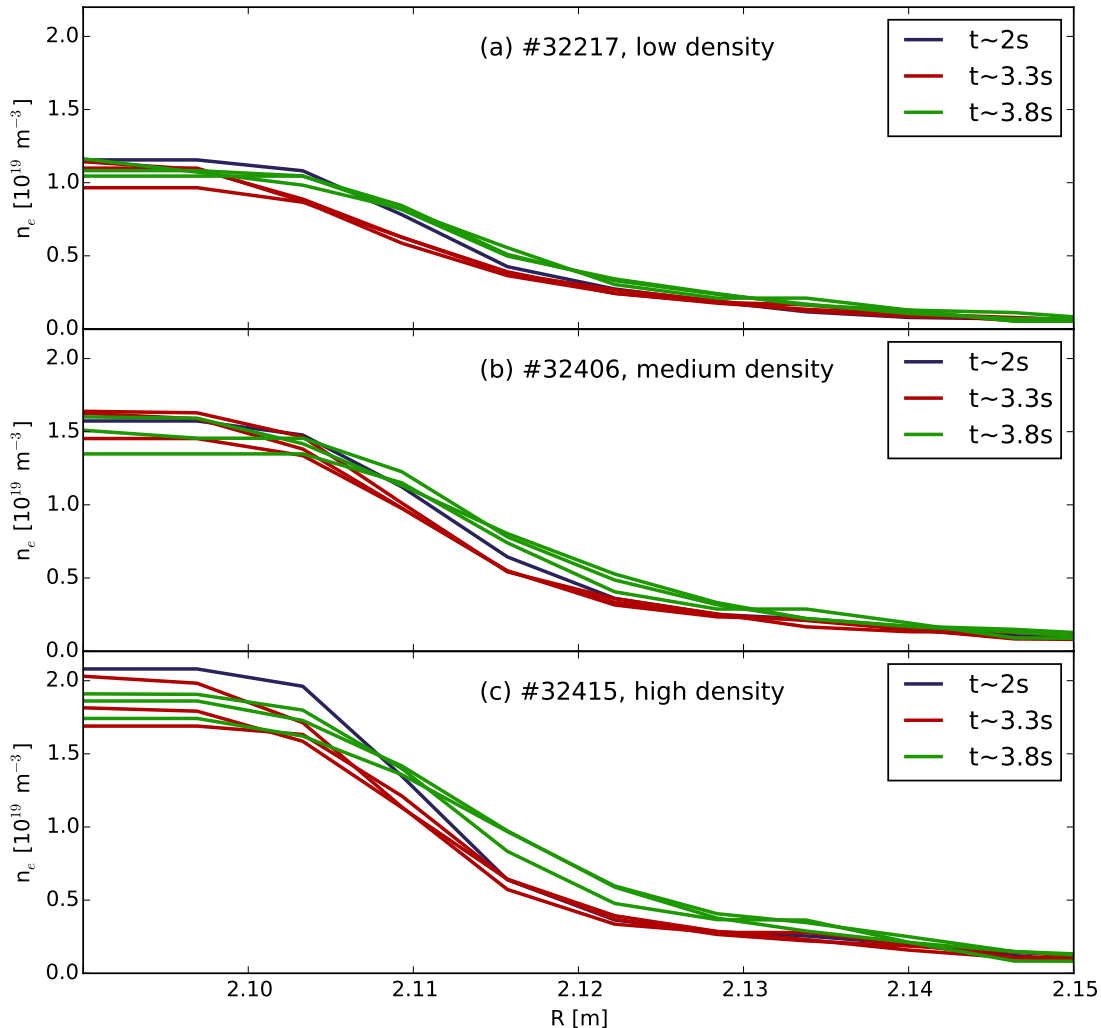


Figure 28: Density profiles at three different time points of three shots with different densities but same $n=2$ coil configuration (see figure 16 for explanation). (a) the low density discharge #32217 as already shown in figure 16. (b) The medium density discharge where the higher density around $n_e=1.5 \times 10^{19} \text{ m}^{-3}$ on the radially inward side is clearly seen. (c) The high density case with a density around $n_e=1.8 \times 10^{19} \text{ m}^{-3}$ inside the Separatrix. In all three shots the radial shift is clearly seen with no distinct dependence on the density.

Figure 29 shows an analysis of the three shots. No change of the amplitude with changing density is observed and good agreement between VMEC and the

measurement for all three cases especially for the high density case is seen.

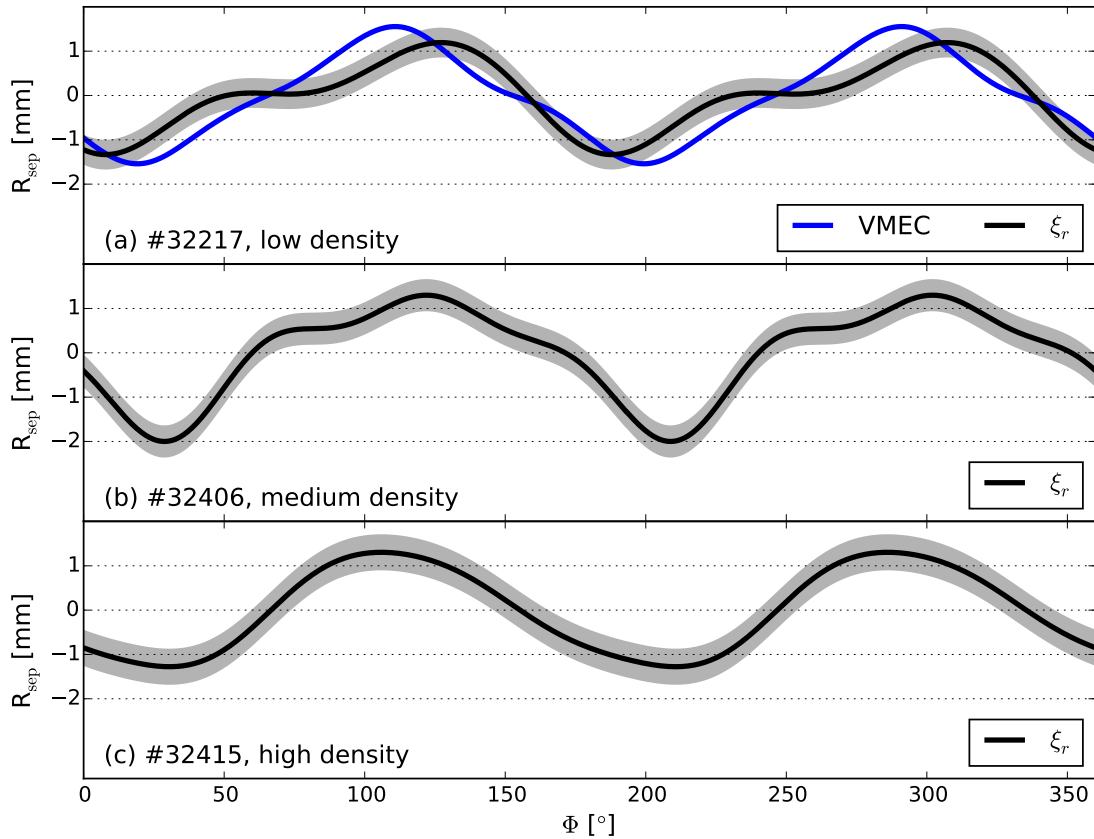


Figure 29: Measurements of the corrugation compared to VMEC simulations for three different density discharges with resonant $n=2$ perturbations. (a) is the low density case as already shown in figure 27 with amplitudes of the measurement of 1.3 ± 0.3 mm and 1.5 mm for the VMEC simulation. (b) shows the medium density case and an amplitude of the measurement of 1.6 ± 0.3 mm. (c) shows the high density case with an amplitude of 1.4 ± 0.4 mm.

6.4 n=1 Comparison

In this chapter two n=1 discharges with different applied perturbation field strengths are compared to investigate the displacement in vicinity of resistive MHD. For the low perturbation field discharge #33189 the current in the perturbation coils is reduced to 250 A in comparison to 1 kA for #33080. Using the full current of the MP-coils, a rotating 2/1 mode is observed (poloidal mode number m=2 and toroidal mode number n=1). Figure 30 shows electron temperature (T_e) profiles of the high perturbation field discharge at three different time points that show profile flattening as an indicator of an island present at approximately $\rho_{\text{pol}}=0.8$. The profiles are flat when measuring the O-point of the island because the field lines around the island work like a shortcut for particles due to the highly increased transport parallel to the field lines. At the X-point the profile shows normal behavior. The mode is rotating with the magnetic perturbations, which translates to 1 Hz for this discharge.

In figure 31 time traces of the electron temperature of different horizontally aligned measurements are shown. It can be seen as a kind of 2D mapping of the magnetic field, the temperature increases with decreasing ρ_{pol} and the time gives the usual toroidal rotation. The X-point of the island can be seen at approx. $t=4.9$ s where the two neighboring channels around 500 eV show a maximum temperature gradient between each other. Before and afterwards the gradients are lower. The 1 Hz modulation can also clearly be seen at higher energies.

The experiments with reduced coil currents are conducted to avoid mode penetration for the investigation of the effect of the mode penetration on the displacement. Figure 32 shows the measured corrugations from the two n=1 discharges. The corrugation of #33189 has been multiplied by 4 due to the different currents in the coils. The VMEC calculations do not agree with the measurements.

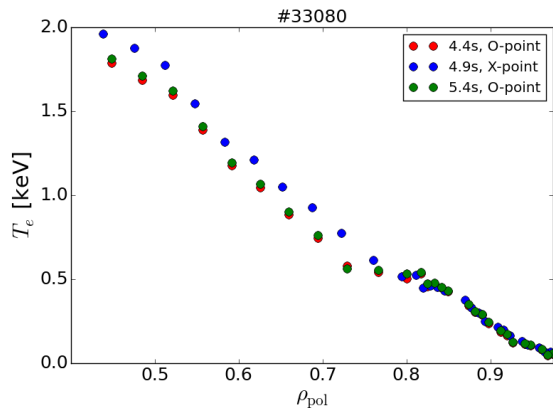


Figure 30: T_e profiles of #33080 [45].

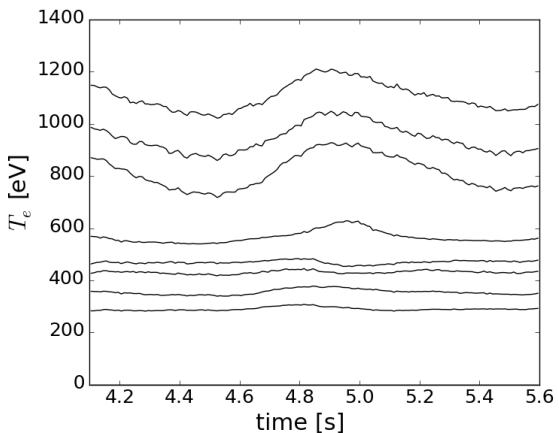


Figure 31: T_e time traces of horizontally aligned measurements for #33080 [45].

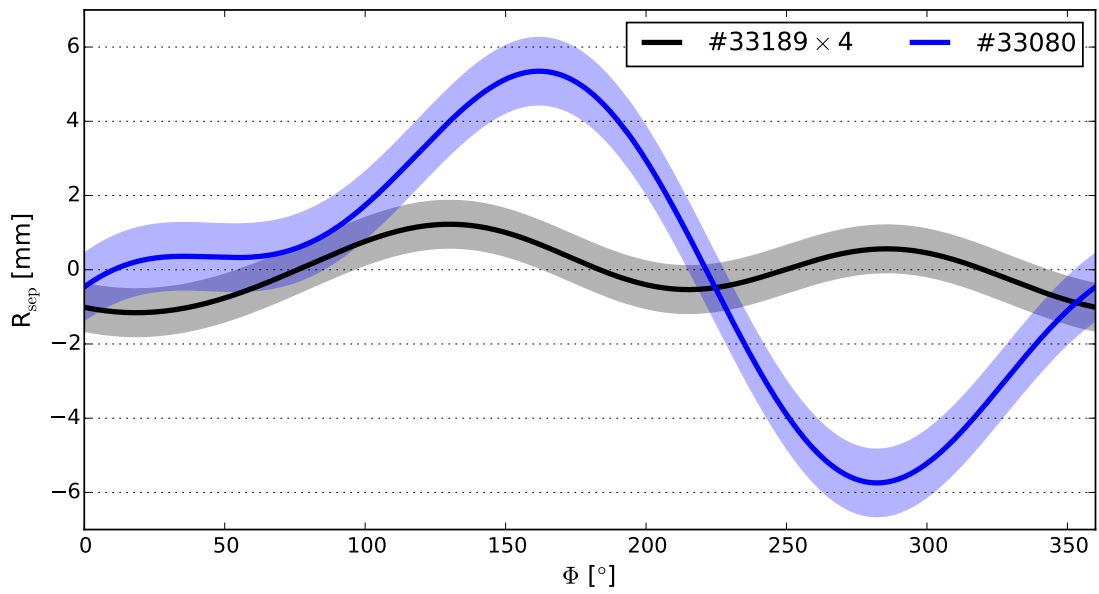


Figure 32: Comparison of the corrugation of the two $n=1$ discharges. The displacement of #33189 in black is multiplied by four to allow for an estimation of the influence of the rotating locked mode, changing the amplitude from 0.3 ± 0.2 mm to 1.2 ± 0.6 mm. In blue the amplitude of the measured displacement of #33080 shows a significantly higher amplitude of 5.6 ± 0.9 mm.

7 Discussion

Summary In this thesis the three-dimensional plasma displacement due to external magnetic perturbations has been measured by the lithium beam while the perturbation was rigidly rotated. The movement due to the plasma control system has been calculated and taken into account by the IDE equilibrium reconstruction using magnetic measurements at two toroidally shifted positions. After the movement due to the control system has been subtracted the displacement of the analyzed discharges was compared to non-linear ideal MHD simulations by VMEC and field line tracing of the vacuum field. VMEC simulations have the advantage of considering ideal MHD effects like screening in comparison to the vacuum field calculations.

Movement of Control System The measured magnetic field in a magnetic probe close to the perturbation coils and the movement due to the control system shows a phase correlation which is consistent for all analyzed shots. Since this probe is used by the FPP diagnostic that is used for the plasma control system it strongly suggests that stray fields influence the position control. It is recommended to exclude this probe from the FPP diagnostic or to consider the perturbation field in the measured field. This could reduce the amplitude of the movement due to the control system significantly. All in all the contribution of the control system is not following a simple pattern. Because it has the same frequency as the displacement it is not visible in the Separatrix traces of a diagnostic at first sight and can amplify or weaken the measured displacement dependent on the position of the diagnostic through constructive or destructive interference.

n=2 For the n=2 discharges a comparison of the measurements to the simulations shows good agreement for the VMEC simulations especially for the fundamental harmonic and reasonable agreement for the vacuum field line tracing. The vacuum field estimation seems to overestimate the amplitude of the corrugation which would indicate that the perturbation fields are damped by the plasma response. Furthermore the vacuum approximation shows a better agreement for the non-resonant cases which indicates a stronger plasma response for the resonant case. A variation of density does not vary significantly the measured plasma response as suggested by measurements of the displacement.

n=1 The presence of a rotating locked mode amplifies the displacement significantly. This indicates that the plasma response due to magnetic perturbations is non-linear in the vicinity of resistive MHD. For both n=1 discharges the vacuum and VMEC simulations show no similarity to the measurements, simulations with resistive MHD codes could potentially lead to better results.

Displacement The amplitudes of the displacement are small compared to the minor radius of ASDEX Upgrade and the highest one was measured in the presence of a 2/1 mode and was approx. 1.1% of the minor plasma radius. If the displacements

for future machines are also in this range it probably won't lead to severe problems concerning minimum wall gaps and safe operation in L-mode.

Outlook For further investigation of the displacement in the future, the measurements could be compared with simulations from other codes that could potentially consider other physical mechanisms, for example the non-linear resistive MHD code JOREK. Another possible extension of the work could be to include measurements of other diagnostics, like the electron cyclotron emission spectroscopy or reflectometry.

A Acknowledgement

An dieser Stelle möchte ich all den Leuten danken, die mir während meiner Masterarbeit, als auch während des ganzen Studiums zur Seite standen.

Allen voran möchte ich mich bei meinen Betreuern bedanken, ohne die diese Arbeit nicht möglich gewesen wäre und die für einen unkomplizierten Ablauf gesorgt haben. Friedrich Aumayr möchte ich dafür danken, dass er sich bereit erklärt hat meine Arbeit zu betreuen und für den Arbeitsplatz den er mir bereitwillig zum abschließenden Schreiben in Wien zur Verfügung gestellt hat. Matthias Willensdorfer dafür, dass er mich durch den Dschungel der Fusionsforschung begleitet und zu jeder Tages und Nachtzeit schnellstmöglich auf meine Anfragen und Mails reagiert hat. Elisabeth Wolfrum dafür, dass sie den Link zwischen TU Wien und IPP hergestellt hat und für ihre ausgezeichnete Betreuung während der vorangegangenen Projektarbeit. An alle drei nochmal ein herzliches Dankeschön! Die finanzielle Unterstützung die ich einerseits vom Max-Planck-Institut für Plasmaphysik und andererseits vom European Fusion Education Network bekommen habe war sehr hilfreich, um mich vorrangig auf die Arbeit konzentrieren zu können. Michael Faitsch möchte ich für das Korrekturlesen der letzten zwei Kapitel danken. Rainer Fischer, Gregor Birkenmeier und Louis Giannone für das Bereitstellen der Daten und der Hilfe zu ihren Diagnostiken. Auch den Doktoranden Dominic, Felician, Stephan, Michael die auf meine Fragen gute Antworten hatten und mit denen ich so manchen lustigen Spieleabend verbrachte, möchte ich danken.

Natürlich seien auch die zahlreichen Bekanntschaften und Freunde in München und Wien erwähnt. Meine (Büro-)Kollegen in Garching Basti, Federico, Georg, Johannes, Marko und Sergiu mit denen ich nicht nur im Institut viel Zeit verbrachte sondern auch außerhalb so manchen Blödsinn unternommen habe. Mein Mitbewohner in München Benni der mich in der Freizeit zum Klettern brachte. In Wien die Mitglieder der AG Aumayr, die mich freundlich aufnahmen und mit denen ich auch so manchen lustigen Abend verbrachte.

Die zahlreichen Freunde die mich während des Physikstudiums begleitet haben allen voran Adrian, Basti, Daniel, Gregor, Jason, Mäx und Sigrid. Auch meinen guten Freunden außerhalb der Physik, die mich nicht nur während der Masterarbeit unterstützt haben, Paul und Markus, möchte ich danken.

Mein besonderer Dank gilt meiner Familie, meinen Eltern, Karin und Christian die mich immer unterstützt haben und zwischendurch so manchen Schlafplatz zur Verfügung gestellt haben. Last but not least, meiner Freundin Giulia die mich immer unterstützt, auch wenn es nicht immer leicht ist, ich hoffe das gleiche für dich zu tun.

B Bibliography

- [1] J. Wesson, D. Campbell, and J. Connor. *Tokamaks. 2* (1997).
- [2] G. Kamelander. *Grundlagen der Plasmatheorie* (2013).
- [3] M. Kikuchi, K. Lackner, and M. Quang. *Fusion Physics*. IAEA pp. 24–26 (2012).
- [4] A. Garofalo, V. Chan, J. Canik, M. Sawan, M. Choi, D. Humphreys, L. Lao, R. Prater, P. Stangeby, H. S. John *et al.* *Progress in the physics basis of a Fusion Nuclear Science Facility based on the Advanced Tokamak concept*. Nuclear Fusion **54**, 073015 (2014).
- [5] T. Pütterich. *Control and Diagnostic of High-Z Impurities in Fusion Plasmas* (2015).
- [6] J. Schweinzer. *Physikalische Grundlagen des Kernfusionsreaktors* (2013).
- [7] F. M. Laggner. *Electron Density Perturbations at the Plasma Edge of the ASDEX Upgrade Tokamak* (2013).
- [8] F. Wagner. *A quarter-century of H-mode studies*. Plasma Physics and Controlled Fusion **49**, B1 (2007).
- [9] P. Snyder, H. Wilson, J. Ferron, L. Lao, A. Leonard, T. Osborne, A. Turnbull, D. Mossessian, M. Murakami, and X. Xu. *Edge localized modes and the pedestal: A model based on coupled peeling–ballooning modes*. Physics of Plasmas (1994-present) **9**, 2037 (2002).
- [10] V. Igochine. *Active Control of Magneto-hydrodynamic Instabilities in Hot Plasmas*. Springer (2015).
- [11] H. Zohm. *The physics of edge localized modes (ELMs) and their role in power and particle exhaust*. Plasma Physics and Controlled Fusion **38**, 1213 (1996).
- [12] J. Connor, A. Kirk, H. Wilson, and S. Benkadda. *Edge localised modes (ELMs): experiments and theory*. In *AIP Conference Proceedings*, vol. 1013, p. 174 (2008).
- [13] T. E. Evans, R. A. Moyer, K. H. Burrell, M. E. Fenstermacher, I. Joseph, A. W. Leonard, T. H. Osborne, G. D. Porter, M. J. Schaffer, P. B. Snyder *et al.* *Edge stability and transport control with resonant magnetic perturbations in collisionless tokamak plasmas*. nature physics **2**, 419 (2006).
- [14] I. Joseph. *Edge-Localized Mode Control and Transport Generated by Externally Applied Magnetic Perturbations*. Contributions to Plasma Physics **52**, 326 (2012).

-
- [15] J. Callen. *Pedestal Structure without and with 3D Fields*. Contributions to Plasma Physics **54**, 484 (2014).
- [16] W. Suttrop, R. Nazikian, and A. Kirk. *Role of plasma shape in access to ELM suppression at low collisionality: First observation of ELM suppression in ASDEX Upgrade in a shape-matching identity experiment with DIII-D*. Bulletin of the American Physical Society (2016).
- [17] M. Willensdorfer, S. Dens, E. Strumberger, W. Suttrop *et al.* *Plasma response measurements of magnetic perturbations using electron cyclotron emission and comparison to 3D ideal MHD equilibrium*. Plasma Phys. Control. Fusion (2016).
- [18] I. Chapman, M. Becoulet, T. Bird, J. Canik, M. Cianciosa, W. Cooper, T. Evans, N. Ferraro, C. Fuchs, M. Gryaznevich *et al.* *Three-dimensional distortions of the tokamak plasma boundary: boundary displacements in the presence of resonant magnetic perturbations*. Nuclear Fusion **54**, 083006 (2014).
- [19] I. Chapman, J. Holgate, N. B. Ayed, G. Cunningham, C. Ham, J. Harrison, A. Kirk, G. McArdle, A. Patel, R. Scannell *et al.* *The effect of the plasma position control system on the three-dimensional distortion of the plasma boundary when magnetic perturbations are applied in MAST*. Plasma Physics and Controlled Fusion **56**, 075004 (2014).
- [20] H. Zohm. *Magnetohydrodynamic Stability of Tokamaks*. John Wiley & Sons (2014).
- [21] H. Zohm. *MHD-Gleichgewichte und Stabilität heißer Fusionsplasmen* (2004).
- [22] J. P. Freidberg. *Ideal MHD*. Cambridge University Press (2014).
- [23] S. P. Hirshman and J. Whitson. *Steepest-descent moment method for three-dimensional magnetohydrodynamic equilibria*. Physics of Fluids (1958-1988) **26**, 3553 (1983).
- [24] S. Hirshman, P. Merkel *et al.* *Three-dimensional free boundary calculations using a spectral Green's function method*. Computer Physics Communications **43**, 143 (1986).
- [25] E. Strumberger, S. Günter, and C. Tichmann. *MHD instabilities in 3D tokamaks*. Nuclear Fusion **54**, 064019 (2014).
- [26] K. H. Finken, S. Abdullaev, M. Jakubowski, M. Lehnen, A. Nicolai, and K. Spatschek. *The structure of magnetic field in the TEXTOR-DED* (2005).
- [27] T. Lunt, Y. Feng, M. Bernert, A. Herrmann, P. de Marné, R. McDermott, H. Müller, S. Potzel, T. Pütterich, S. Rathgeber *et al.* *First EMC3-Eirene simulations of the impact of the edge magnetic perturbations at ASDEX Upgrade compared with the experiment*. Nuclear Fusion **52**, 054013 (2012).
- [28] T. Evans. *Resonant magnetic perturbations of edge-plasmas in toroidal confinement devices*. Plasma Physics and Controlled Fusion **57**, 123001 (2015).

-
- [29] A. Herrmann and O. Gruber. *ASDEX Upgrade-Introduction and overview*. Fusion Science and Technology **44**, 569 (2003).
- [30] B. Streibl, P. T. Lang, F. Leuterer, J.-M. Noterdaeme, and A. Stabler. *Machine design, fueling, and heating in ASDEX upgrade*. Fusion science and technology **44**, 578 (2003).
- [31] W. Suttrop, M. Rott, T. Vierle, B. Streibl, A. Herrmann, V. Rohde, U. Seidel, D. Yadikin, O. Neubauer, B. Unterberg *et al.* *Design of in-vessel saddle coils for MHD control in ASDEX Upgrade*. In *Proc. 35th EPS Conf. on Plasma Physics (Hersonissos, Crete, 2008)*, vol. 32 (2008).
- [32] W. Suttrop, L. B. Orte, R. Fischer, J. Fuchs, R. McDermott, H. Muller, T. Put-terich, S. Rathgeber, E. Viezzer, E. Wolfrum *et al.* *Access conditions for ELM mitigation with non-axisymmetric magnetic perturbations in ASDEX Upgrade*. In *39th EPS Conference on Plasma Physics and 16th International Congress on Plasma Physics*. European Physical Society (2012).
- [33] W. Suttrop, A. Kirk, R. Nazikian, N. Leuthold, E. Strumberger, M. Willensdorfer, M. Cavedon, M. Dunne, R. Fischer, S. Fietz *et al.* *Experimental studies of high-confinement mode plasma response to non-axisymmetric magnetic perturbations in ASDEX Upgrade*. Plasma Physics and Controlled Fusion **59**, 014049 (2016).
- [34] W. Suttrop. *private communication* .
- [35] *Documentation of the Lithium Beam Diagnostic*. https://www.aug.ipp.mpg.de/documentation/pub/Diagnostics/LithiumBeam/Li_Injector.jpg (2017).
- [36] M. Willensdorfer, E. Wolfrum, R. Fischer, J. Schweinzer, M. Sertoli, B. Sieglin, G. Veres, and F. Aumayr. *Improved chopping of a lithium beam for plasma edge diagnostic at ASDEX Upgrade*. Review of scientific instruments **83**, 023501 (2012).
- [37] J. Schweinzer, F. Aumayr, P. Platzer, M. Schneider, D. Wutte, and H. Winter. *Two programs for calculations of collisional atomic data for lithium beam plasma spectroscopy*. Computer physics communications **88**, 83 (1995).
- [38] P. Platzer. *Bestimmung von Z_{eff} in Fusionsplasmen mittels Lithiumstrahl-*diagnostik** (1994).
- [39] R. Fischer, E. Wolfrum, J. Schweinzer *et al.* *Probabilistic lithium beam data analysis*. Plasma Physics and Controlled Fusion **50**, 085009 (2008).
- [40] V. Mertens, G. Raupp, and W. Treutterer. *Plasma control in ASDEX Upgrade*. Fusion science and technology **44**, 593 (2003).
- [41] W. Schneider, P. McCarthy, K. Lackner, O. Gruber, K. Behler, P. Martin, and R. Merkel. *ASDEX Upgrade MHD equilibria reconstruction on distributed workstations*. Fusion Engineering and Design **48**, 127 (2000).

-
- [42] R. Fischer, C. Fuchs, B. Kurzan, W. Suttrop, E. Wolfrum, and A. U. Team. *Integrated data analysis of profile diagnostics at ASDEX Upgrade*. Fusion science and technology **58**, 675 (2010).
- [43] R. Fischer, A. Bock, M. Dunne, J. Fuchs, L. Giannone, K. Lackner, P. McCarthy, E. Poli, R. Preuss, M. Rampp *et al.* *Coupling of the flux diffusion equation with the equilibrium reconstruction at ASDEX Upgrade*. Fusion Science and Technology **69**, 526 (2016).
- [44] E. Strumberger. *Finite- β magnetic field line tracing for Helias configurations*. Nuclear Fusion **37**, 19 (1997).
- [45] M. Willensdorfer. *private communication* .